Full length article

A novel genetic expression programming assisted calibration strategy for discrete element models of composite joints with ductile adhesives

Xing-er Wang [a,b,c], Armin Yousefi Kanani [a], Kai Pang [a], Jian Yang [b,c,d], Jianqiao Ye [a], Xiaonan Hou [a,*]

[a] *School of Engineering, Lancaster University, Lancaster, LA1 4YW, UK*
[b] *State Key Laboratory of Ocean Engineering, Shanghai Jiao Tong University, Shanghai 200240, PR China*
[c] *Shanghai Key Laboratory for Digital Maintenance of Buildings and Infrastructure, School of Naval Architecture, Ocean and Civil Engineering, Shanghai Jiao Tong University, Shanghai 200240, PR China*
[d] *School of Civil Engineering, University of Birmingham, Birmingham B15 2TT, UK*

ARTICLE INFO

ABSTRACT

Discrete element (DE) model has a great feasibility in modelling the microstructural behaviours of adhesive composite joints. However, it demands a sophisticated calibration process to determine microscale bond parameters, which involves massive efforts in both experimental and numerical investigations. This work developed a novel calibration strategy based on DE models and genetic expression programming (GEP) approach for predicting the behaviours of hybrid composite joints encompassing the material nonlinearity, large ductile deformation and multiple fracture modes. In the developed strategy, both the bulk and interlaminar-like properties of ductile adhesives were concerned to suit various joint configurations. GEP modelling was performed based on the datasets from virtual DE experiments. Symbolic regression models were subsequently developed to facilitate the parameters determination. A series lab tests were conducted to validate the numerical results. It shows that the calibrated DE model can adaptively simulate the featured behaviours of both the ductile adhesive and composite joints with different configurations well in most examined occasions. Therefore, it could be suggested to generalize the developed strategy in the development of other DE models for saving the massive efforts in the calibration process of microstructural parameters.

1. Introduction

The worldwide targets of carbon emission reduction lead to a significant demanding of reducing the weight of industrial products. Adhesive hence becomes increasingly popular in the industry to make lightweight products as it is capable of bonding different materials with lower weight cost [1,2]. For instance, in the automotive industry, it is reported that the brittle epoxy and the ductile polyurethane (PU) adhesives will have significant increase of their use in vehicles. The typical use is adhesive joining [3]. Many efforts have been made to facilitate the structural performance of adhesive joints, which requires satisfactory abilities of strength and ductility [4,5]. High strength adhesive can provide better load bearing performance whereas it usually presents unfavourable brittleness [6,7]. Ductile adhesive can promote the deformation compatibility between different materials in scenarios such as temperature actions [8]. However, it might also be with lower strength. The designs and the improvement technology of the adhesive joints hence require a thorough investigation of their failure mechanisms [9].

The primarily key factors influencing the failure mechanism are the mechanical performance of selected adhesives as well as their co-performance and compatibility with the adherends [10–12]. Katsivalis et al. [13] tested the adhesive system encompassing glass, steel and brittle, ductile adhesives. It is found that the glass failure might be preceded by damages at the interface with strong and brittle adhesive. An alternative case using intermediate strength adhesive presented a glass failure before debonding or the cohesive failure of adhesives, when ductile adhesives was adopted. Banea et al. [14] experimentally investigated the influences of multi-material adherend (high strength steel (HS), aluminium (AL) and carbon fibre reinforced plastics (CFRP)) and geometrical design on the strength of adhesive joints. It is found that the structural PU adhesive can fully function to final adhesive yielding when using similar CFRP adherends, whereas its efficiency decreases for dissimilar adherends, particularly for the design of unbalanced adherend thicknesses.

The mechanical performance of adhesive is also highly sensitive to the temperature, load conditions and load rate [15–18]. Marchione [19] experimentally examined the influence of high temperature on

---

* Corresponding author.
  E-mail address: x.hou2@lancaster.ac.uk (X. Hou).

the static and cyclic response of glass–aluminium joints. The double lap joints were tested under a high temperature of 85 °C and heating–cooling cycles. The results identify the positive effect of heating–cooling cycles on the mechanical performance, whilst the prolonged heat action may yield negative effect on the failure mode. The joints on marine top coats using PU, polysiloxane and epoxy were found to have high mechanical stability after accelerated ageing including spray exposure, heat cyclic and high moisture [20]. The rate dependent behaviour of adhesive was examined in Lißner's work [21]. The results have a similar trend to the findings of other polymers that the adhesives are likely to have higher failure strength and reduced ductility under a high load rate [22,23].

In addition, two factors, i.e. the surface treatment of adherend [24, 25] and adhesive thickness [26], are worthy of investigation as they are also highly related to the joint failure. The former leads to the variation of surface roughness and interfacial microstructures [27], whilst the latter is found to greatly affect the fracture toughness as it influences the local fracture process zone or plastic zone size [28, 29]. Therefore, when numerical attempts are conducted to predict the failure mechanism of adhesive joints, there should be a thorough consideration of key factors. The popular finite element (FE) model combined with updated technologies such as virtual crack closure technique (VCCT) [30,31] and cohesive zone model (CZM) [32–34] can be easily adopted to simulate the variation of constitutive behaviours of adhesives and adherends. However, it exhibits difficulties in modelling the microstructural response and has limitation in adaptively describing the influences due to the adhesive thickness without performing more lab tests to identify the cohesive parameters [29]. For example, the complex distribution of voids inside adhesive and the micro-roughness at adhesion interface is very difficult to develop in FE model using CZM.

An alternative numerical solution is the discrete element method (DEM), which has strength in describing the microscale, microstructural and discontinuous behaviours of materials [35,36]. Particle based DEM are more frequently used in the current reports to represent the bulk objects, e.g., Marini [37] used DEM to simulate the shot peening process on sharp notches, in which the impactors were also simplified into particles. With introducing the microscopic contact or bond models between particles, particle based DEM can also provide a universal model for various types of material behaviours [38]. Most efforts of DEM focus on modelling brittle materials [39,40] as the classic contact models do not allow for a softening behaviour whilst the particles are assumed to be rigid. Efforts have been made to develop new formulations or constitutive laws for the particles or contact/bond models to enable DEM to suit more complex material properties [41]. Rojek et al. [42] developed the formulations and numerical algorithms for the deformable particles and the associated nonlocal contact model. Gibaud [43] developed a pairwise attractive and repulsive bond model to simulate the irreversible strain accumulation of materials under compression. The large deformation can be well captured after a calibration of numerical parameters to approximate viscoplastic Norton law. However, the calibration of the microscopic discrete element (DE) parameters is complex, particularly when attempting to achieve a high consistency of many macroscopic properties. As for the ductile adhesive joint, both the calibrations of bulk properties and interlaminar-like properties should be performed to achieve accurately universal solutions. Once the interfacial property between adherend and adhesive can be estimated, multiple failure modes, e.g., adhesive failure, cohesive failure and mixed mode failure, can be captured by a DE model.

This work seeks a novel calibration strategy that can save many efforts to rapidly develop particle based joint models, as the first attempt of this kind. The proposed strategy and the calibrated DE model have the following novelty points:
(1) The calibration strategy introduces machine learning based approach to find simplified symbolic regression (SR) models, which are able to simplify the complex property calibration of particle based joint model. The strategy can be extended and covers a wide range of materials for joints.

(2) A sequential calibration procedure of bulk and interlaminar-like properties is proposed, which can accurately capture the nonlinear behaviours of ductile adhesive and its fracturing performance in the joints;
(3) The developed model can adaptively describe the variation of failure mechanism and joint strength without conducting more lab tests to extract the cohesive parameters of different design variables such as adhesive thickness. The developed model can further be updated with considering the microstructural features of adhesive joints.

To achieve the above novelties, this work firstly adopted a combined DE and GEP approach to find the SR models to calibrate the microscopic parameters, which can reproduce the bulk and interlaminar-like properties of ductile adhesives in different joint designs. Virtual numerical experiments using DE method were conducted to provide adequate datasets to run the GEP modelling, which aimed to obtain the SR models. Uniaxial tensile (UT) test, double cantilever beam (DCB) test, end notched flexure (ENF) test and single lap joint (SLJ) test using the selected adhesive, polyurethane (PU, Teroson MS 9399), were conducted to validate the developed DE model with the characterized parameters of adhesive.

2. Methodology

The principles of primary approaches involved in this work, discrete element method and genetic expression programming, were described here. It is followed by showing the concept and the process of developing the calibration.

2.1. Discrete element method (DEM)

DEM was originally developed by [44] for modelling discontinua which can be represented by discrete balls or discs. The finite displacement and rotation of particles are allowed in DEM. The model is able to automatically locate the updating contacts or separations between particles. In this work, particle flow code (PFC) software [45] was employed to perform the simulation. It utilizes an explicit and time-marching algorithm to solve the equations. The motion equations can be described by the resultants of the force and the moment of force between the contacted particles, which can be calculated by [46]:

$$\text{Linear motion} \qquad m_i \frac{d^2 \mathbf{x}_i}{dt^2} = m_i \mathbf{g} + \sum_{j=1}^{n} \mathbf{F}_{ij} \qquad (1)$$

$$\text{Rotational motion} \qquad I_i \frac{d\boldsymbol{\omega}_i}{dt} = \sum_{j+1}^{n} \mathbf{r}_i \times \mathbf{f}_{ij} \qquad (2)$$

where t is time, m_i is the particle mass, $\mathbf{x}_i$ is the displacement vector. $\mathbf{F}_{ij}$ is the force vector at normal contact, $\mathbf{g}$ is the vector of gravitational acceleration, n is the number of particles contacted. I_i is the mass moment of inertia, $\boldsymbol{\omega}_i$ is the vector of angular velocity. $\mathbf{r}_i$ denotes the radius vector of the ith particle, $\mathbf{f}_{ij}$ is the frictional vector between the ith and jth particles. The subscript i refers to the ith particle being contacted, j indicates the jth particle contacting with the ith particle.

Contact models with different separation–traction laws can be assigned between neighbouring particles to simulate the solid materials [47]. The bond models can be represented as the elements (e.g., springs, dashpots) distributed at the contact point or surface (Fig. 1(a)). For example, parallel bond model (PBM) has been frequently used to describe the quasi-brittle material [39]. As for those ductile or soft materials, soft bond model (SBM) which allows for the softening phase of contact law is more suitable and hence is used to simulate adhesives here.

In the built-in SBM in PFC, the mathematical descriptions of several microscale parameters used in the subsequent study should be clarified. For the defined contact stiffness k_n, k_s, the effective modulus E_m can be obtained by:

$$\text{Effective modulus} \qquad E_m = k_n(r_i + r_j) \qquad (3)$$
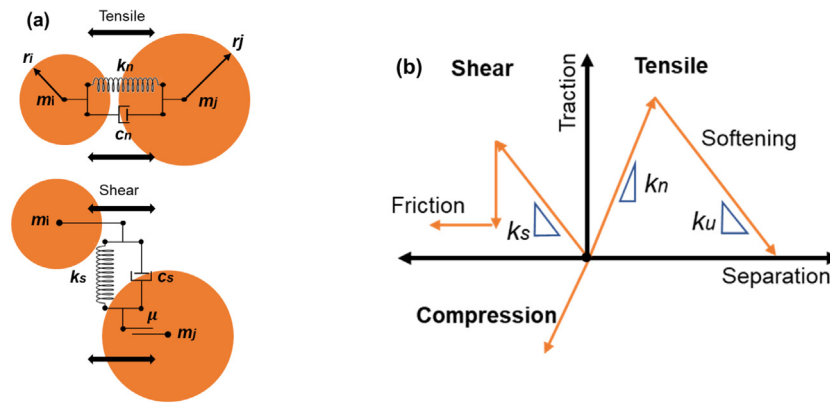
Fig. 1. Schematic diagrams of contact model: (a) a typical representation of contact between ith and jth particles in normal and tangential direction, k is the contact stiffness, c is the contact damping. The subscripts n, s denote the normal and tangential directions, respectively. μ is the friction coefficient. (b) The contact law of soft bond model. k_u is the softening stiffness.

where r_i and r_j are the particle radius of ith and jth particle, respectively. The contact area radius can be adjusted using the radius multiplier m via $\bar{r} = m\min(r_i, r_j)$, when evaluating the criteria of bond failure.

As shown in Fig. 1(b), once the tensile stress at contact surface exceeds the defined tensile strength f_n, the contact law enters into a softening stage with the softening stiffness k_u. The softening factor ζ (sb_factor) can be calculated by $\zeta = k_n/k_u$. If $\zeta \to 0$, the contact will transform into a perfectly brittle one. If the bond has not failed under tension, the shear strength $f_s = c - \sigma_n \tan\phi$ is evaluated, where σ_n is the normal stress at contact, c is the cohesion strength, ϕ is the friction angle. Once shear failure occurs, the contact is assigned with a frictional strength.

2.2. Genetic expression programming (GEP)

Machine learning models such as neural-based models [48] and genetic algorithms (GA) [49] are popular in recent years as it might be able to locate the implicit correlations between various factors which are difficult to be identified using traditional engineering theories [50]. Related works to the parameter identifications or optimizations can be frequently found. For instance, Mani et al. [51] conducted a thorough analysis on the tensile properties of stainless steel-based dissimilar joints, which adopted different process parameters to describe the welding. GA was then used to optimize the process parameters. GA shows the ability to facilitate the estimation of heterogeneous parameters and hence was used. This work seeks a practical approach to estimate the selections of the adjustable microscopic parameters based on the experimental data. Thus, in addition to obtaining the SR models for roughly predicting the target properties, the contribution of each parameter to the concerned macroscopic property should be examined as well to give guidance on the determination procedure of the adjustable parameters.

SR model aims to find a function $f(X) = Y'$, which can achieve the minimum deviation between the predicted property Y' and the target property Y. X denotes the datasets of adjustable parameters. The regressed model is determined through the continuous optimization until reaching the best fit. The model is based on the symbols from the predefined space of mathematical expressions.

Genetic programming (GP) algorithm is considered as an originally evolutionary based predictive machine learning method. It has been widely used in finding the optimized regression model in a wide range of topics, e.g., geotechnics related problems [40]. Reports concerning its use in predicting the failure strength [52] and mixed mode behaviours of adhesive joints [53] can also be found. In this study, GEP, a variant of GP algorithm developed by Ferreira [54] was adopted to find the best fit through employing the crossover and mutation of function structures [55].
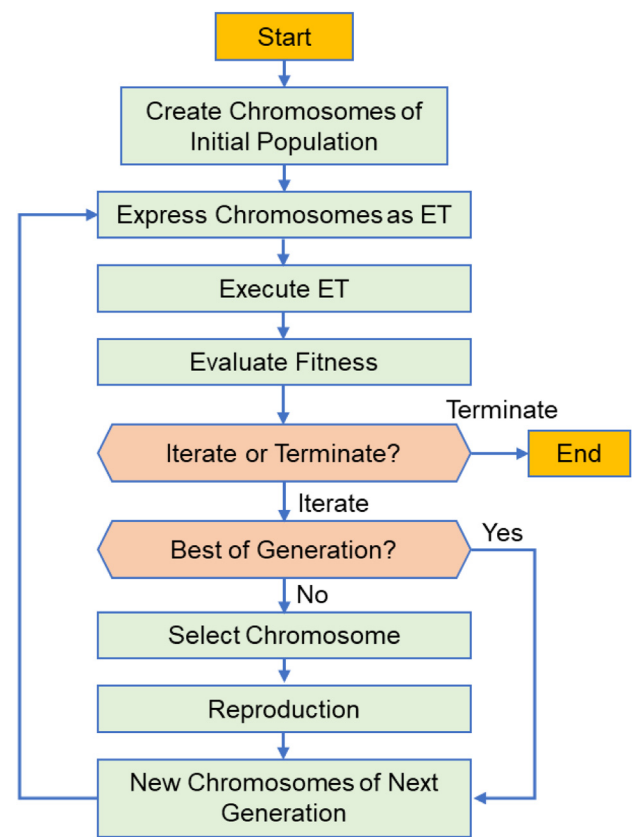

Fig. 2. The flow chart of GEP model.

GEP algorithm encodes the individuals as the linear strings of fixed length (chromosomes), which are subsequently expressed as the nonlinear entities of various sizes and structures (i.e. expression trees, ET). The GEP structure has two components, a head with function symbols and terminal symbols (e.g., selected microscopic parameters), a tail having terminal symbols. GEP modelling starts with the stochastic generation of the chromosomes of the initial population. The chromosomes are subsequently translated and expressed. It is followed by the evaluation of the fitness of each individual solution. The procedure will be looped until reaching a defined number of generations or finding a reliable solution (Fig. 2).

The operations such as mutation and crossover in GEP are similar to those in GA algorithm. Fig. 3(a) and (b) give the examples
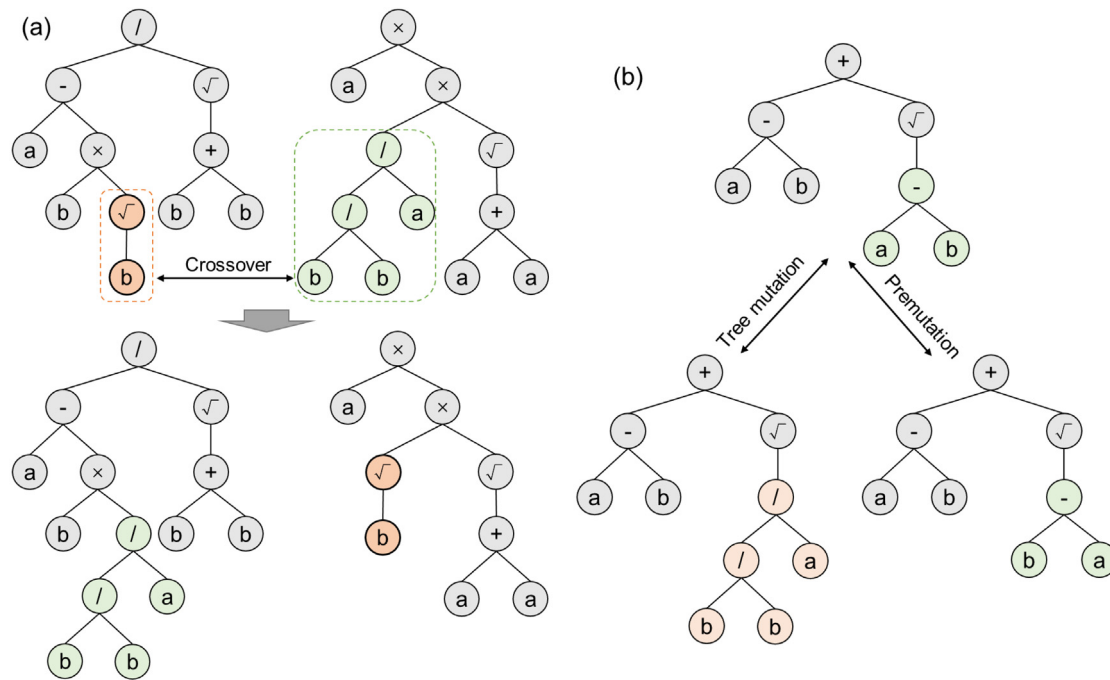
Fig. 3. The crossover and mutation of individuals in GEP model: (a) The crossover of the trees (in dash labels). (b) The tree mutation and premutation.

of crossover and mutation operations, respectively. In Fig. 3(a), two individuals $(a - b\sqrt{b})/(\sqrt{b+b})$ and $a((b/b)/a)\sqrt{a+a}$ transform to $(a - (b((b/b)/a)))/(\sqrt{b+b})$ and $a(\sqrt{b}\sqrt{a+a})$ via crossover operation, respectively. The variables a and b can refer to the selected microscale parameters in soft bond model. The individuals can further be combined using mathematical symbols to obtain a final model. Through the model procedure shown in Fig. 2, the SR models that correlate the input variables (microscale parameters) and predicted outputting results (macroscale properties) can be obtained.

2.3. Calibration strategy with combined DE-GEP

The calibration procedure using combined DE and GEP method has two primary parts, which sequentially obtain the SR models to predict the bulk properties and interlaminar-like properties. The microscopic parameters of soft bond model for adhesives can be determined by fixing the most significant parameters in SR models to these properties and a subsequent refined adjustment to optimize the overall performance. The detailed strategy of calibration with combined DE–GEP is shown in Fig. 4.

The GEP modelling for obtaining predictive SR models are subjected to many rounds of evaluation on their applicability. The input datasets $\mathbf{D} = (\mathbf{X_0}, \mathbf{Y_0})$ and $\mathbf{D'} = (\mathbf{X'_0}, \mathbf{Y'_0})$ are divided randomly into training and validation parts for the model evaluation. The input dataset encompasses the part $\mathbf{X_0}$ of the selected microscopic parameters (e.g., radius multiplier $\bar{r}$, effective modulus E_m) and $\mathbf{Y_0}$ of the determined target macroscopic properties (e.g., the failure stress, the secant modulus of adhesives). During the training and validation process, the fitness function with root mean square error (RMSE) is defined to evaluate the results from current SR models, as:

$$\text{Fitness function} \qquad \text{RMSE} = \sqrt{\frac{1}{N} \sum_{\bar{j}=1}^{N} (f(x_{\bar{i}\bar{j}}) - y_{\bar{j}})^2} \qquad (4)$$

where $f(x_{\bar{i}\bar{j}})$ is the predicted value by chromosome $\bar{i}$ according to current SR model, $y_{\bar{j}}$ denotes the extracted target property in dataset $\mathbf{Y_0}$. Other performance indexes such as the coefficient of determination are also used to assess the predictive model. The suitable SR model will be selected once its performance is satisfactory with low system error.

Finally, if the SR models are determined, the calibration can continue following the defined procedure in Fig. 4.

3. Calibration of bulk property

Bulk property, a fundamental property of adhesive, should firstly be calibrated. Two aspects are considered. First, in certain practices, thick adhesive might be used to connect components, e.g., PU or ionomer adhesive to bond glass products [56]. The mechanical performance of this connection can be well predicted with adopting the bulk property. Second, it is of significance to introduce the fundamental bulk property such as elastic modulus to generate more realistic traction–separation law of a very thin ductile adhesive layer in a joint, e.g., a trapezoidal law. Combined DE–GEP modelling was adopted here to find practical formulas to promote the calibration.

3.1. DE modelling of uniaxial tensile tests

Three characteristic properties, tensile strength (f_t), the strain at tensile strength (ε_p, refers to peak strain in the following context) and secant modulus at the strain of 0.1 (E_s), were treated as the target properties for regression. A virtual DE experiment of UT tests on the ductile adhesive specimens was conducted using particle flow code (PFC) software [45]. The virtual specimen was determined as the core area of actual dumbbell adhesive specimen, which was designed according to the testing standard EN ISO 37 [57]. In order to describe a more realistic fracturing path inside adhesive particles, the adhesive particles were generated using random particle generation and the expansive particle packing method. The UT model had a size of 20 mm × 5 mm. The soft bond model was used to bond the particles to describe the nonlinearity and the softening behaviours of ductile adhesives.

Many microscopic parameters in the soft bond model can be adjusted to cover a wide range of material behaviours. Eleven soft bond parameters were selected, in which four parameters were assigned with constant values (Table 1) after preliminary trials. To provide adequate sampling range of target properties, the remaining parameters were assigned within the defined range of values in Table 2. The rational range of microscopic parameters is important to obtain more reliable SR models. It is suggested that this range should firstly be classified into
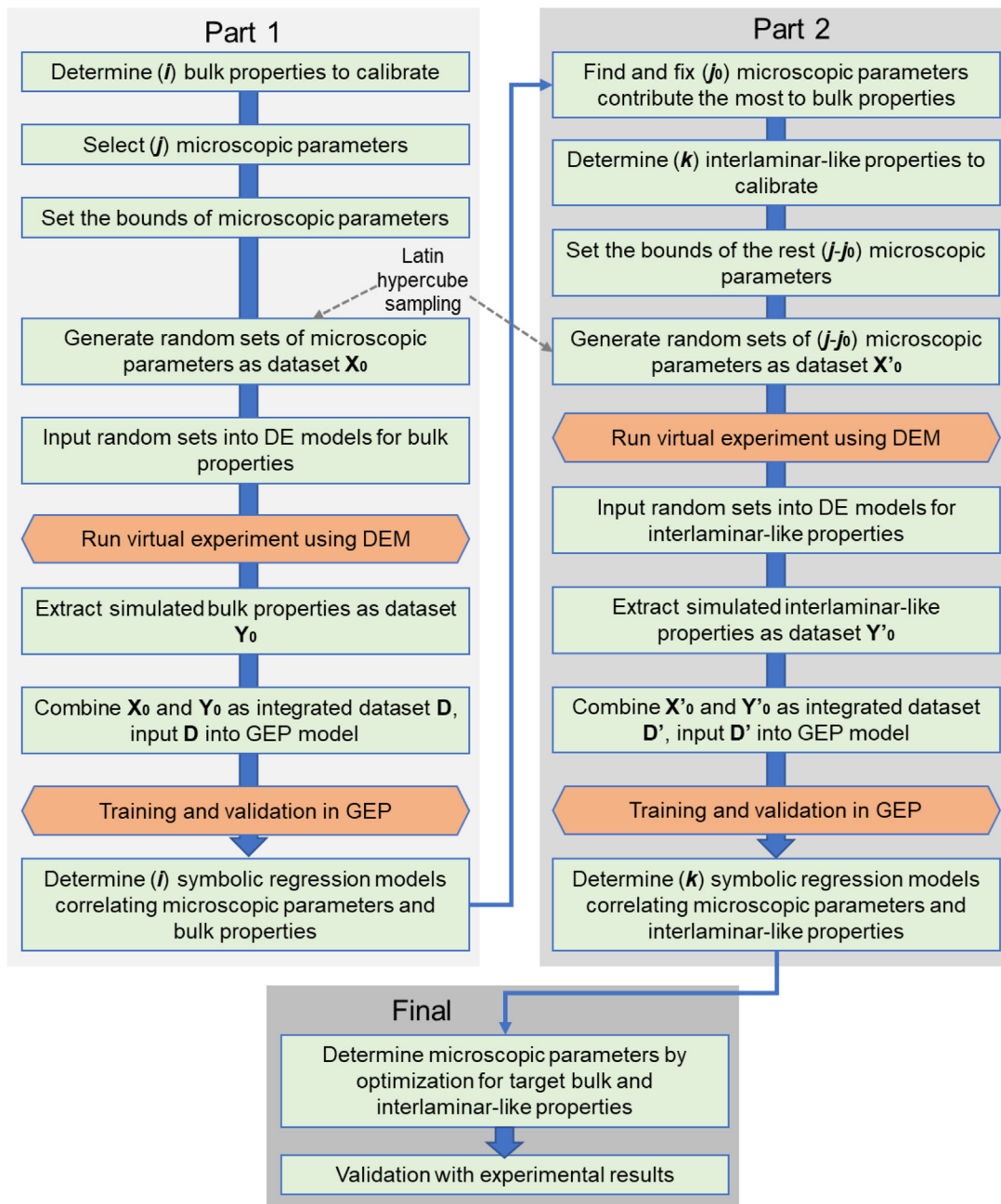
Part 1

Determine (*i*) bulk properties to calibrate

Select (*j*) microscopic parameters

Set the bounds of microscopic parameters

Generate random sets of microscopic parameters as dataset **X₀**

Input random sets into DE models for bulk properties

Run virtual experiment using DEM

Extract simulated bulk properties as dataset **Y₀**

Combine **X₀** and **Y₀** as integrated dataset **D**, input **D** into GEP model

Training and validation in GEP

Determine (*i*) symbolic regression models correlating microscopic parameters and bulk properties

Part 2

Find and fix (*j₀*) microscopic parameters contribute the most to bulk properties

Determine (*k*) interlaminar-like properties to calibrate

Set the bounds of the rest (*j-j₀*) microscopic parameters

Generate random sets of (*j-j₀*) microscopic parameters as dataset **X'₀**

Run virtual experiment using DEM

Input random sets into DE models for interlaminar-like properties

Extract simulated interlaminar-like properties as dataset **Y'₀**

Combine **X'₀** and **Y'₀** as integrated dataset **D'**, input **D'** into GEP model

Training and validation in GEP

Determine (*k*) symbolic regression models correlating microscopic parameters and interlaminar-like properties

Latin hypercube sampling

Final

Determine microscopic parameters by optimization for target bulk and interlaminar-like properties

Validation with experimental results

Fig. 4. The detailed procedure of DEM calibration assisted by GEP. The symbols in brackets denote the number of the following variables.

Table 1
Fixed parameters of standard DE model.

ID	Keyword	Description	Values
1	porosity	Porosity of packing particles	0.1
2	sb_soft	Softening factor	100
3	sb_cut	Softening Tensile strength factor	0.9
4	sb_fa	Friction angle (°)	30

Table 2
Adjustable parameters of standard DE model.

ID	Symbol	Keyword	Description	Range
1	E_m	sb_emod	Effective modulus (MPa)	(1, 6)
2	K	sb_kratio	Normal to shear stiffness ratio	(1, 10)
3	m	sb_rmul	Radius multiplier	(0.2, 2)
4	fr	sb_ref_str	Reference strength of soft bond (MPa)	(1, 10)
5	r_{min}	rmin	Minimum particle radius (mm)	(0.05, 0.2)
6	α_a	alpha_a	Ratio of maximum to minimum particle radius	(1, 1.5)
7	β	beta	Ratio of tensile to cohesion strength	(0.1, 1)

brittle and ductile categories. A larger interval of parameters can subsequently be estimated based on the selected adhesive. This is due to the finding that a general solution of symbolic regression model is unlikely to work for both brittle and ductile adhesives. The classification based on the brittle or ductile features can greatly facilitate the applicability of the obtained predictive model. More information on the range can be found in Ref. [58]. Note that the tensile strength of bond is set as half of reference strength.

The datasets for performing the following GEP modelling include the adjustable parameters as the input variables and the extracted target properties from DE simulation as the predicted output. Increasing
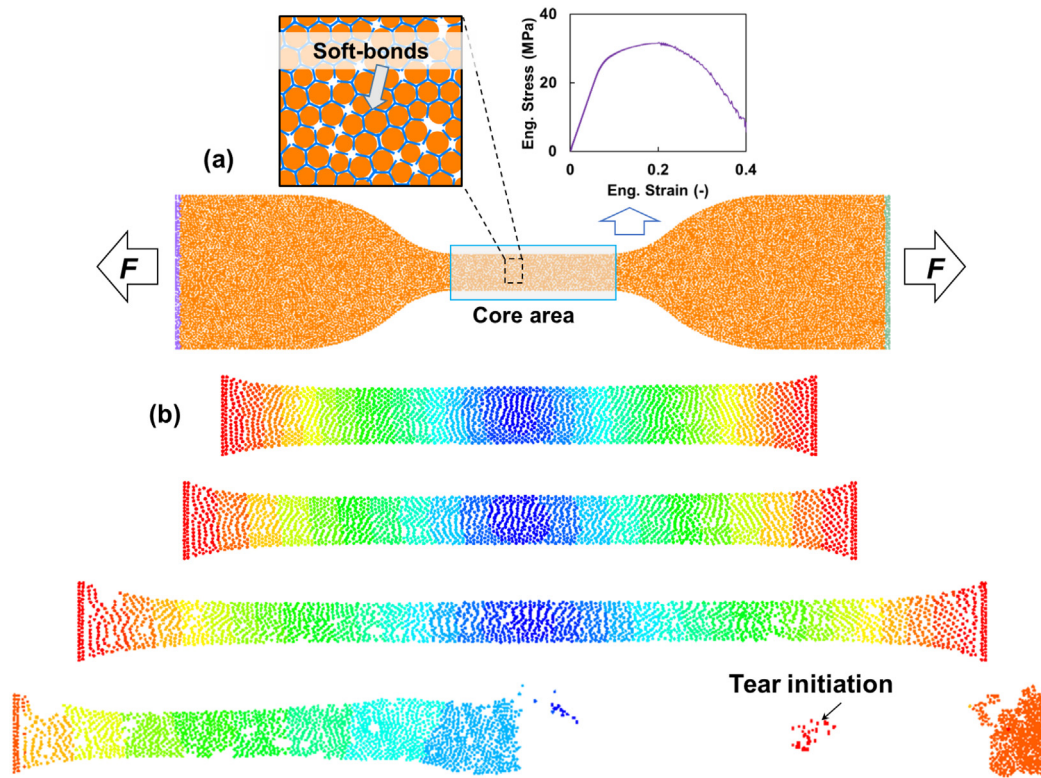
Fig. 5. Standard DE model of uniaxial tensile test on adhesives: (a) the schematic of DE model with random particle packing, (b) an example case of ductile adhesive, showing the ability of DE model to simulate large deformation.

the number of datasets and a fine distribution of the input variables can facilitate the reliability of the regressed model. Latin Hypercube Sampling (LHS) method was then employed to generate a fine distribution of the adjustable parameters within the defined range. 300 groups of parameter sets were created for the UT specimens.

The standard UT specimen after the expansive particle packing and the assignment of the soft bonds between the neighbouring particles is shown in Fig. 5(a). Two layers of particles at the edges acted as the grip, which had a constant load speed of 0.1 m/s after a sensitivity study of load speed. An example of the deformation process and the tensile failure was given in Fig. 5(b). It is seen that the assigned parameter set is able to trigger typical deformation and tearing of ductile adhesives.

The collections of engineering stress–strain relationships from the virtual experiments of ductile adhesives were shown in Fig. 6. Several specimens can reach a strain more than 4.0 when tearing occurs. It is found that with the assigned range of the adjustable parameters the target tensile strength varies from 0.3 MPa to 11.4 MPa, the strain at tensile strength is within 0.1–5.6, the secant modulus has a range of 0.4–13.9 MPa. It can be concluded that through assigning appropriate parameters and bond models, the particle packing can well model the tensile behaviour of ductile materials, showing its ability to model a flexible range of materials.

3.2. GEP modelling and validation

The datasets of bulk property had 300 groups of data including the adjustable parameters and the corresponding target properties from DE modelling. 2/3 of the datasets were randomly selected to perform the training whilst the other datasets were used for validation. Table 3 gives the configuration of the GEP algorithm and the activated mathematical symbols in this study.

The comparison between the target properties and predicted results of the SR model by GEP algorithm is shown in Fig. 7. Linear fitting is used to fit the data. It can be seen that most of the SR models can
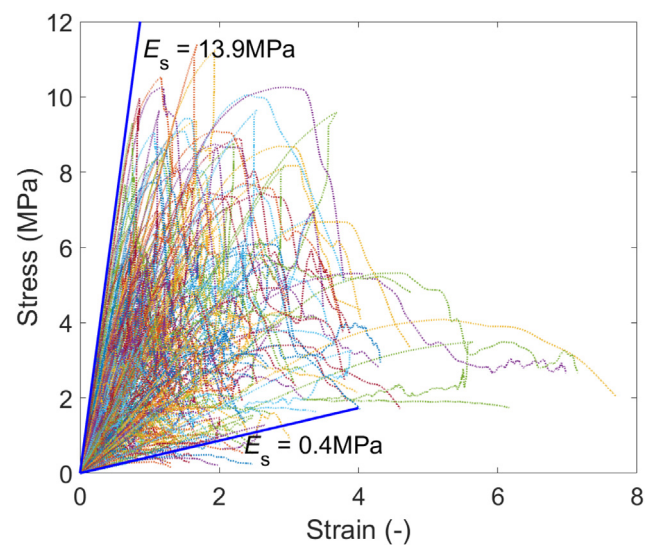

Fig. 6. Stress–strain results of DE virtual experiment. The upper and lower bounds of secant modulus were given.

Table 3
Configuration of GEP algorithm.

Parameters	Value (range)
Number of chromosomes	30
Head size, number of genes	8, 3
Training/Validation records	200/100 (total 300)
Enabled symbols	$+, -, \times, /, e^x, 10^x, \ln x, \lg x, |x|, 1/x, x^i,$ $\sqrt[i]{x}(i = 2, 3, 4 \dots), \tanh, \tan^{-1}$

obtain a value of R^2 over 0.92, indicating a satisfactory prediction. The predicted tensile strength and secant modulus of ductile adhesives
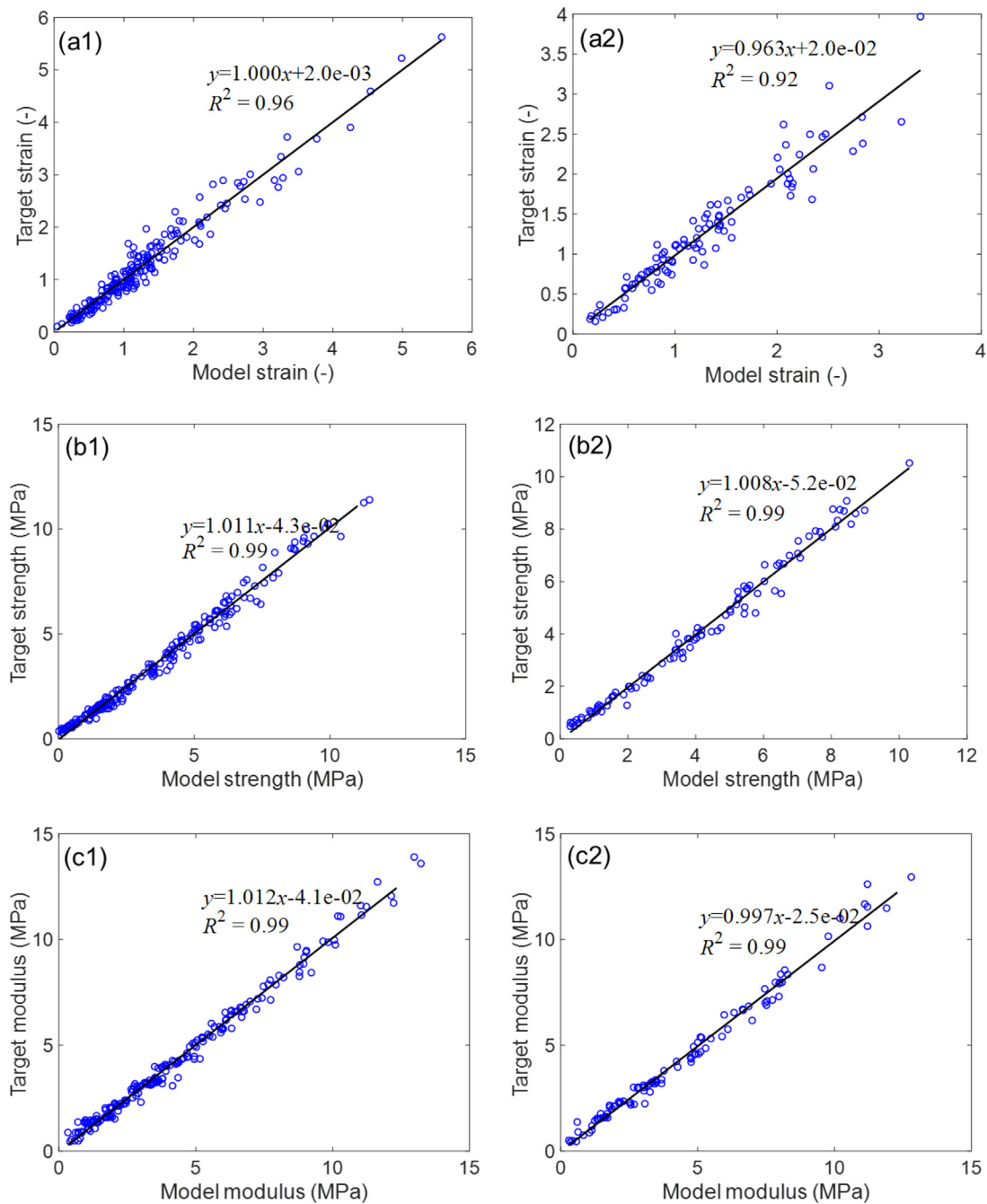
Fig. 7. Comparison of target and predicted results for ductile adhesives: training and validation results of peak strain (a1, a2), tensile strength (b1, b2) and secant modulus (c1, c2). Higher coefficient of determination R^2 indicates better prediction accuracy.

(Fig. 7(b, c)) are found to show a great consistency with actual results. However, note that several data points of peak strain (Fig. 7(a)) exhibit higher dispersion from the actual results, particularly when validating the predicted strain over 2. The dispersion is very likely to be caused by the set-up of the measure points on the virtual UT specimens. Once the tearing position of adhesive is near the measure points in certain cases, the extracted strain results are odd. The adhesives with very large failure strain were seen to result in those odd data points more frequently.

3.3. SR model of bulk property

The determined SR models for the bulk property of ductile adhesives are given in Eqs. (5)–(7). The units of the adjustable parameters are identical to those in Table 2.

Peak strain, (–)

$$
\begin{aligned}
\varepsilon_c = {} & \ln(10^{(0.585 f_r \tan^{-1}(\alpha_a))}) / \ln(10^{E_m}) \\
& + \alpha_a^{\ln K \sqrt{(\beta/m)}} / \ln 10 \\
& - (\sqrt{e^{\beta E_m/4}/f_r})^{1/4}
\end{aligned}
\tag{5}
$$

Tensile strength, (MPa)

$$
\begin{aligned}
f_t = {} & (\ln(f_r + (0.528^{E_m} K)^{0.419 E_m}) / \ln 10)^4 \\
& + \ln((2.2\alpha_a)^{5/3}/e^{m(1-f_r)}) / \ln 10 \\
& + \ln f_r{}^m \ln 10 - \tan^{-1}(K^{1/5} - m)
\end{aligned}
\tag{6}
$$

Secant modulus at strain of 0.1, MPa

$$
\begin{aligned}
E_s = {} & E_m + E_m/(1.57K) \\
& + 1 - \left| (1 - m/0.975)^2 - e^{(\alpha_a - 1.1)} \right| \\
& + \ln m^{\ln(1.8+m)^{E_m}}
\end{aligned}
\tag{7}
$$

Table 4
Assigned values of adjustable parameters for ductile adhesive.

Symbol	Keyword	Values	Symbol	Keyword	Values
E_m	sb_emod	1.0 MPa	r_{min}	rmin	0.1 mm
K	sb_kratio	3.6	α_a	alpha_a	1.33
m	sb_rmul	1.8	β	beta	0.25
fr	sb_ref_str	2.1 MPa			

Table 5
Interfacial properties (Teroson MS 9399) extracted from actual experiment.

Property	Symbol	AL–AL	PPA–PPA
Normal fracture energy	G_{IC} (N/mm)	2.11 ± 0.27	0.95 ± 0.12
Tangential Fracture energy	G_{IIC} (N/mm)	6.50 ± 0.20	4.1 ± 0.50
Normal fracture strength	σ_n (MPa)	2.52 ± 0.45	0.65 ± 0.24
Tangential fracture strength	σ_t (MPa)	6.67 ± 0.25	3.5 ± 0.20

In order to investigate the contribution of each parameter to the target property, six parameters were selected to perform the correlation study. β was not introduced as it was a parameter controlling the shear strength in the soft bond model, which was originally not related to the tensile property. It was considered as one key parameter in the study on coordinating the interlaminar-like property afterwards. The parameters were assigned with a constant value respectively if they were not the examined one. The examined ones were within the ranges in Table 2. Table 4 gives the constant values of the parameters which do not act as the examined ones.

The calculated ranges of the target properties, peak strain, tensile strength and secant modulus at the strain of 0.1 in ductile adhesives were shown in Fig. 8(a1–a3), (b1–b3), (c1–c3), respectively. The projections on the planes with the constant maximum assigned values of the examined parameters were also added to better illustrate the correlation trends (see contours without mesh grid). From Fig. 8, the finding can be concluded as:

(1) Peak strain, the parameters, f_r and E_m, present a maximum strain increment of 5.55 and 1.12, respectively. The parameters m, α_a have negligible effects on the peak strain.

(2) Tensile strength, f_r and m can generate a strength increment up to 10.9 MPa and 10.24 MPa, respectively. E_m, K, α_a can be omitted when calibrating the tensile strength.

(3) Secant modulus at strain of 0.1, E_m and m can generate peak modulus increment of 11.9 MPa and 2.36 MPa, respectively. The stiffness ratio K is also seen to have an interval of modulus increment, (0.57 MPa, 3.44 MPa). f_r and α_a does not show significant influences on the secant modulus.

(4) The minimum particle radius is not included in the equations. Thus, it is implied that r_{min} cannot facilitate the calibration of the target properties of ductile adhesives.

Once the target properties are determined from the experiment, it is suggested that the secant modulus should be firstly calibrated as it also acts as a key factor to achieve a satisfactory separation–traction law through a combined performance of the adhesive deformation and tearing. The parameters contribute the most can be adjusted and fixed firstly to get a value near the target property. The remaining parameters can then be used to slightly refine the target property and overall the similar macroscopic behaviours of the calibrated adhesive.

3.4. Validation of parameters for bulk property

In order to provide experimental data for determining the microscopic parameters, UT tests were subsequently conducted to record the stress–strain relationships of adhesives. Ductile polyurethane (PU, Teroson MS 9399), was used to make dumb-bell shaped UT specimens following the ISO 37 [59] standard. Digital image correlation (DIC) technique was used to measure the strain field of the adhesive specimens. The universal tensile machine Instron 3345 was used to perform the tensile tests on the specimens, which was equipped with a 500N load cell for the PU specimens. Three specimens were tested to guarantee the repeatability.

The microscopic parameters for modelling the bulk behaviour of Teroson MS 9399 were calibrated based on the developed SR models and characterization procedure. The calibrated parameters are given in Table 4. The simulated tensile behaviour of the ductile adhesive was compared with those from the experiment, as can be seen in Fig. 9. Note that the odd post-peak curve was resulted from the rapid deformation of teared adhesive. It shows that the calibrated microscopic parameters for the example adhesive are reliable.

4. Characterization of interlaminar-like property

The current reports show that the bulk property cannot be directly used to simulate the interlaminar-like behaviours of adhesive joints with a very thin adhesive layer. For example, the fracture energy of bulk adhesive is commonly greatly higher than that of thin adhesive. Therefore, after calibrating the bulk property, the calibrated parameters should be further coordinated with the interlaminar-like property of thin adhesive in joints. A similar approach of combined DE–GEP modelling was used to find the SR models of interlaminar-like property as well. Fracture energy which dominants the failure strength of the adhesive joint [60] was selected as the calibrated interlaminar-like property.

4.1. DE modelling for determining interlaminar-like property

The experiment on the interlaminar-like behaviour of laminates using Teroson MS 9399 was conducted to provide reference data. Considering that the adherend stiffness and the adhesive thickness will influence the interlaminar-like property such as fracture energy. A fixed configuration with aluminium (AL) adherends and 0.56 mm thick adhesive was used. Classic characterization tests, DCB and ENF, were adopted to obtain the Mode I and Mode II interfacial properties, respectively. The extracted properties were given in Table 5. The interfacial properties between Teroson MS 9399 and Polyphthalamide (PPA) materials, which would be involved afterwards were also given. More information can be found in Ref. [61].

4.2. GEP modelling

The interlaminar-like property is expected to be calibrated without a significant variation of determined parameters for bulk property. However, it is found to be extremely difficult in reaching this aim. The following strategy was adopted: the parameters related to the elastic behaviour were fixed, whilst the adhesive strength was allowed to vary. This strategy has the priority to calibrate the fracture energy.

The discussion on the correlation of parameters to the target property concludes that the parameters E_m (effective modulus) and m (radius multiplier) have significant influence on the secant modulus, they were then fixed. K (normal to shear stiffness ratio) and fr (reference strength) present less influence on the tensile elasticity and hence were adopted as adjustable parameters for interlaminar-like property. β (the ratio of tensile to cohesion strength) has negligible effect on the tensile property of bulk adhesive, it was also selected as it can contribute to the Mode II fracture behaviour of the thin adhesive joint.

GEP modelling was used to obtain the SR models of Mode I and Mode II fracture energies, based on the adjustable parameters (K, fr, β). Through trial tests, the parameters K, β were assigned with a range of (1, 10) and (0.2, 3.0), respectively. The reference strength fr had a range of (0.5, 3). The other parameters were identical to those in Table 4. LHS method was adopted to produce 100 groups of parameters to perform the virtual tests based on the models from Fig. 10.

The separation-fracture energy curves from the virtual experiments on ductile adhesives were given in Fig. 11. The Mode I and Mode II fracture energies of Teroson MS 9399 adhesive were given as reference data. Mode I and Mode II fracture energies in the datasets can reach up to 9.72 N/mm and 31.5 N/mm, respectively. The ranges of the fracture energies can cover the data from the commonly used adhesives and are
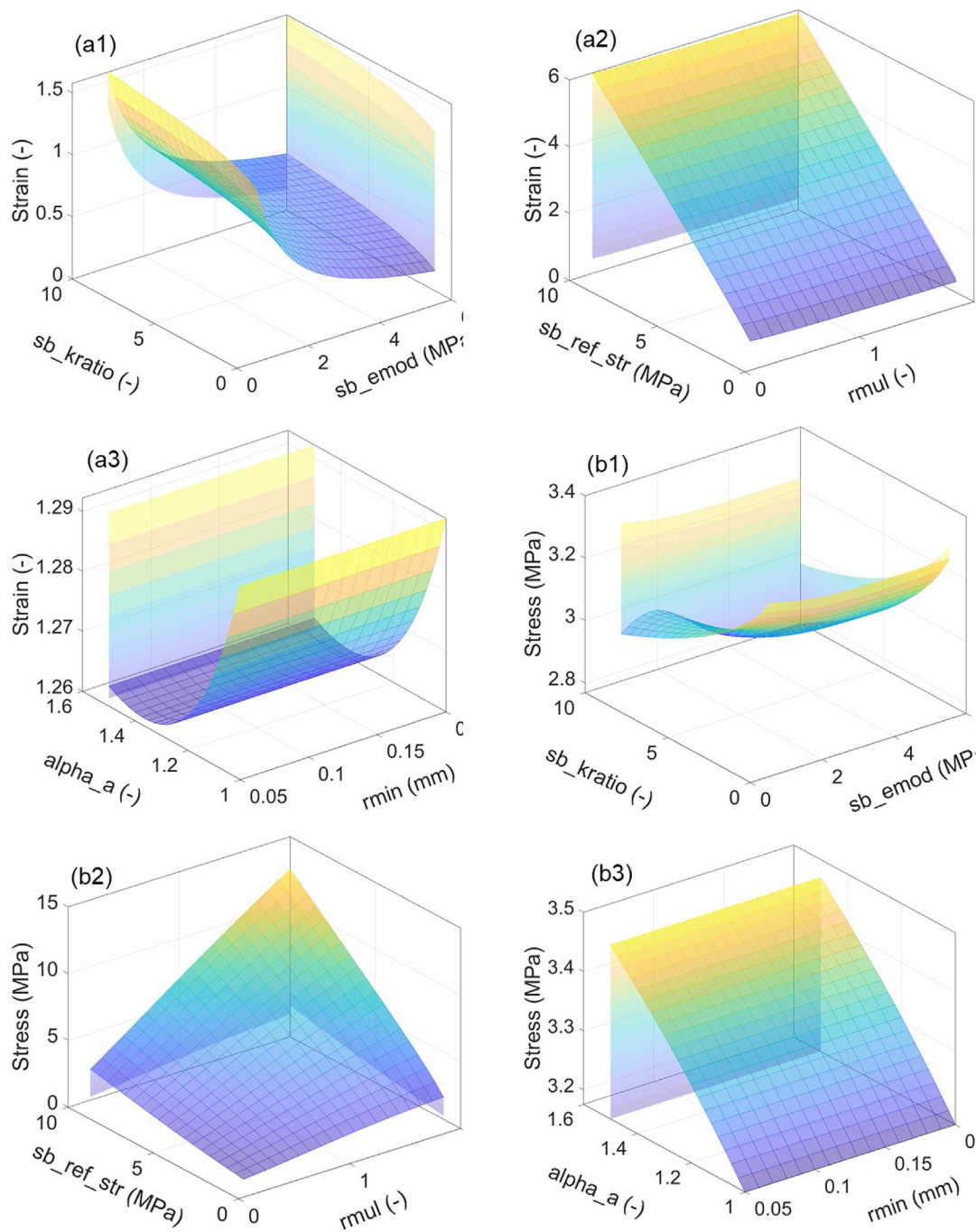
Fig. 8. Predicted results using the regression formulas of ductile adhesives: the peak strain variation by adjusting K and E_m (a1), f_r and m (a2), α_a and r_{min} (a3); the tensile strength variation by adjusting K and E_m (b1), f_r and m (b2), α_a and r_{min} (b3); the secant modulus variation by adjusting K and E_m (c1), f_r and m (c2), α_a and r_{min} (c3). This indicates the contribution of each parameter to the target property.

able to be used in the subsequent GEP modelling. The configuration of GEP model was same as that in Table 3, except for that the training and validation records were 100.

Fig. 12 shows the training and validation of the regressed models. It is found that great difficulties arise in obtaining a satisfactory SR model of ductile adhesives, even the odd results were removed from the dataset (e.g., two models with highest G_{IIC} in Fig. 11(b2)). From Fig. 12(a1, a2), although the values of R^2 are 0.95 in training and 0.9 in the validation of Mode I fracture energy, the results over 2 N/mm are also seen with evident scattering. Similar results are seen in those of

Mode II fracture energy in Fig. 12(b1, b2), this might lead to more trials of determining rough combinations of parameters for the following fine adjustment. Efforts have been made to optimize the SR models of ductile adhesives, however, the limitations of the adopted soft bond models are believed to result in such shortcoming when modelling soft materials and will be discussed in the validation section afterwards.

Furthermore, it is worth noting that the Mode II fracture energy was calculated based on a threshold of declining to 10% of the peak stress. It is found that before the post-peak stress decreasing to the threshold, the shear stress might reach a stress plateau over the threshold with several
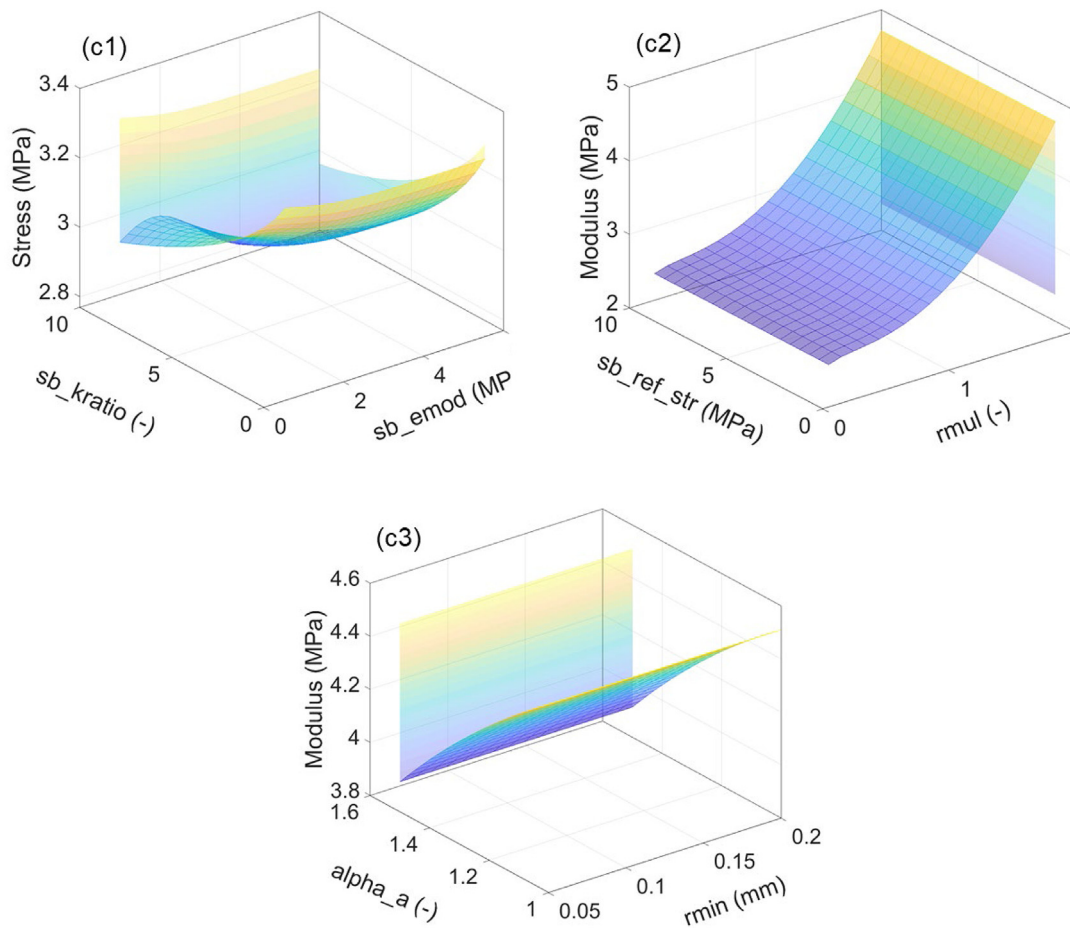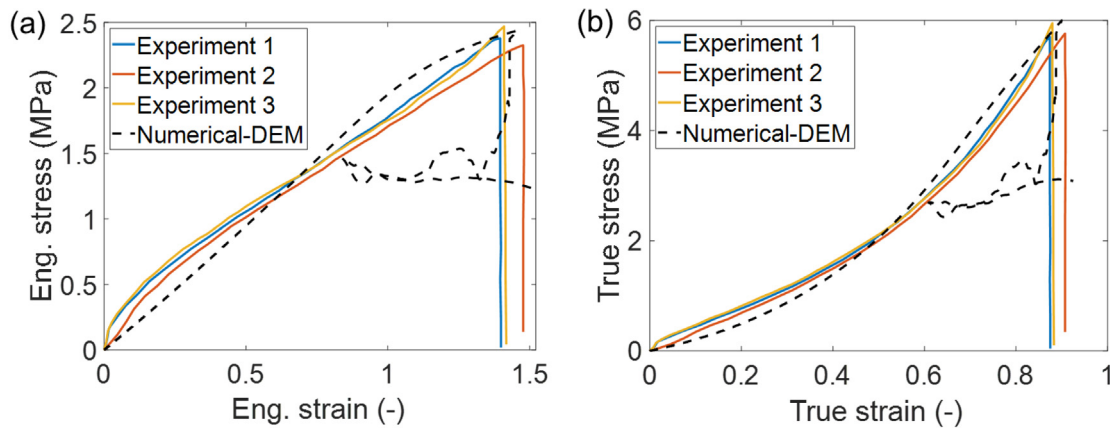
Fig. 8. (*continued*).

Fig. 9. Comparison between the numerical and experimental results of adhesives. Numerical result shows the rapid deformation recovery after tearing: (a) Results of engineering stress and strain. (b) Results of true stress and strain.

parameter combinations. The fracture energy will accumulate with the development of this plateau. It indicates that artificially determined threshold might make incorrect predictions of fracture energy. However, as the computation cost is extremely high if a very small value of threshold is adopted, in most cases of parameters, the threshold of 10% was seen to be adequate to obtain a relative accurate fracture energy. This might also facilitate the data scattering.

The SR models of normal and tangential fracture energies are given as:

$$G_{\mathrm{IC}} \text{ (N/mm)} \quad \begin{aligned} G_{\mathrm{IC}} &= \left| (-2.65 f_{\mathrm{r}}) + \beta^3 \right| / (\beta + 1.5) \\ &+ (-2.29\beta) - e^{-1.57} + (f_{\mathrm{r}} - 0.12)(3.27 - \beta) \\ &- \left| (K/0.6 + \beta - 7 - (K + 0.73)/\beta)^{1/3} \right| \end{aligned} \quad (8)$$
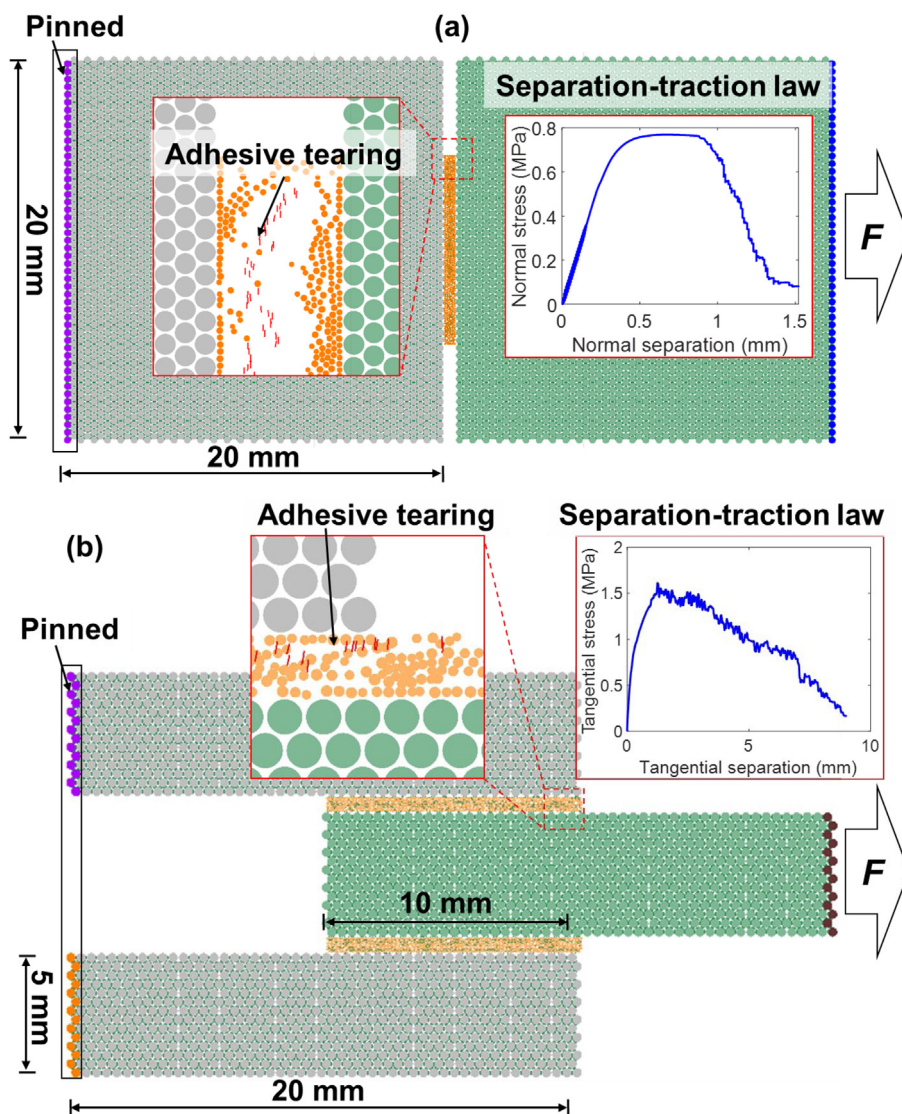
Fig. 10. DE models for the calibration of interlaminar-like property: (a) Model for normal interlaminar-like property, a trapezoidal separation–traction law in normal direction can be achieved with the ductile adhesive. (b) Model for shear interlaminar-like property, which shows a separation–traction law similar to triangular one.
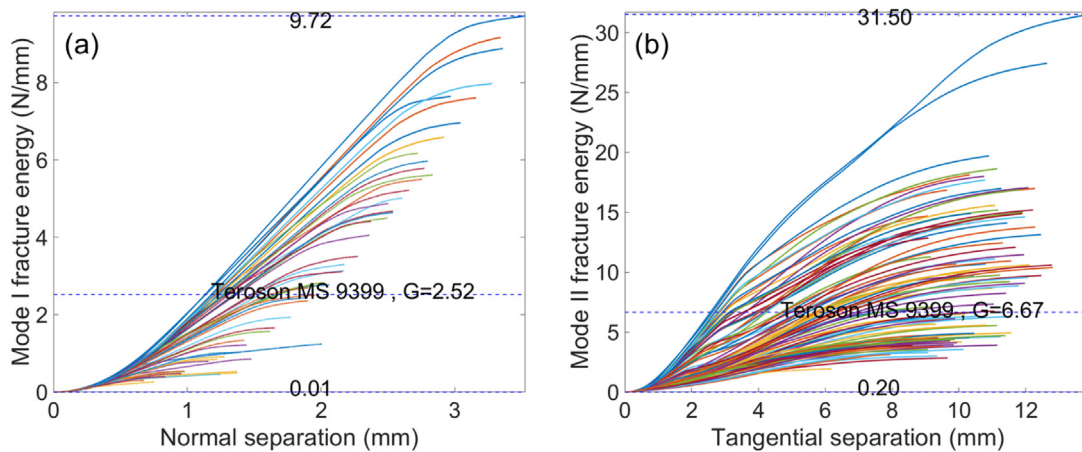

Fig. 11. Separation-fracture energy results of ductile adhesives: (a) Normal direction, (b) Tangential direction. The tested fracture energies of Teroson MS 9399 adhesive were given as reference.
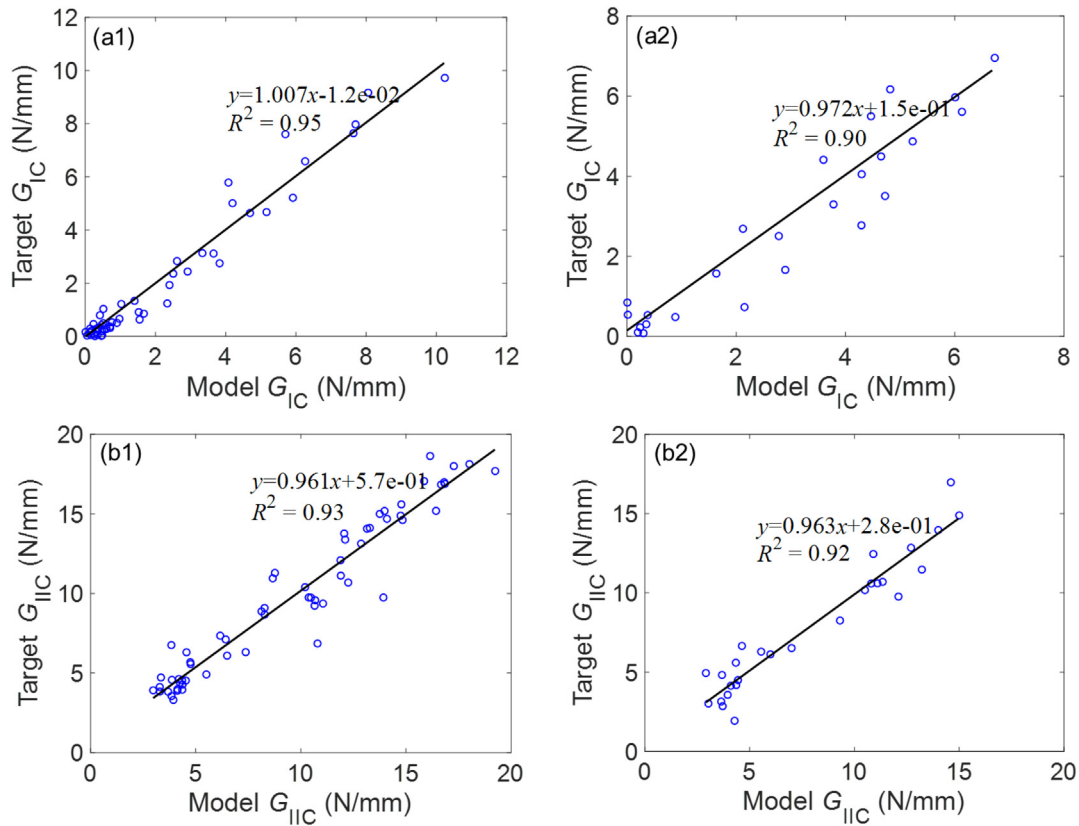
Fig. 12. Target and predicted results for interlaminar-like property of ductile adhesives: training and validation results of Mode I fracture energy (a1, a2), Mode II fracture energy (b1, b2).

$$G_{IC} \text{ (N/mm)} \qquad \begin{aligned} G_{IIC} &= 2.88/\left| (f_r{}^\beta - 4.36 + K + f_r)^{1/9} \right| \\ &+ \beta + \left| e^{f_r} \right| / (\beta^{1.62} + 0.92) \\ &- 7.94/\left| (\beta^{f_r}/f_r)^{\beta^5/5} \right| + \ln(\beta^{-2.74}/K^{f_r})/\ln 10 \\ &+ (f_r - K)/5.78^\beta \end{aligned} \qquad (9)$$

4.3. Parameters determination and validation

(1) DCB, ENF tests with Mode I and Mode II behaviours

Following the regressed models, through a further refinement of parameters, the characterized parameters for Teroson MS 9399 adhesive: stiffness ratio $K = 3.6$, the reference strength $f_r = 1.42$ MPa, strength ratio $\beta = 0.25$. It can be seen that there is no evident adjustment of parameters when comparing with the original values for bulk property. This is due to the greater deformability and low modulus of the selected adhesive, which is less influenced by the fracture process zone. If a stiffer ductile adhesive is used, the characterization for the interlaminar-like property might cost more efforts.

DCB and ENF tests were adopted to validate the characterized parameters for thin adhesive made of 0.56 mm Teroson MS 9399 adhesive. Three specimens were tested for each testing type. More experimental information can be found in Ref. [61]. Fig. 13 shows the DE models of DCB and ENF tests. The load speed was 0.05 m/s after a sensitivity study on load speed. Hexagonal packing with soft bond model was employed for the adherend (AL) in this model, in which the parameters were calculated based on the theoretical solutions in Ref. [62].

The comparison of experimental and numerical results in DCB and ENF tests is shown in Fig. 14(a) and (b), respectively. The load–displacement curve of numerical result in Fig. 14(b) also agrees well

with that of testing data in the aspects of pre-peak growth and peak load. The DE simulation presents a premature decline of load force which might be caused by its higher overall stiffness of adhesive. As shown in Fig. 9(b), the overall stiffness of the PU adhesive in DE model is, in fact, higher than the experimental value because of the nonlinearity of stress–strain relationship. In summary, the overall load–displacement curve of DCB test from DEM simulation is seen to be consistent with experimental data.

As for the ENF test on the PU adhesive, it is found that the DE model presents an incorrect growth of load–displacement relationship (Fig. 14(b)). This is originally resulted from the limitation of the adopted soft bond model in modelling the compressive behaviour of very soft materials. The adhesive particles in ENF test are also subjected to compression when the load head moves downward, which results in the squeezing of particles (see red box in Fig. 14(b)). In fact, the adhesive is incompressible and the particles should be assigned with high penalty stiffness under compression, which is not available by using the soft bond model. The other available contact/bond models cannot well describe the softening and nonlinearity of ductile adhesives and are hence not suitable for the concerned ductile adhesive in this work as well. In addition, it is clarified that the ENF testing results show that the adherend reaches plastic deformation at a displacement of nearly 4 mm. The data after this point cannot be considered if ENF tests aim to capture a perfect Mode II fracture mode. However, the validation of ENF test aims to present the flaw of the developed model in simulating compressive action on soft adhesive. It, in fact, achieves the primary target and also identifies the plastic deformation of adherend, which can be seen that the numerical result declines at a similar displacement to the testing data because of the plastic deformation of adherends (Fig. 14(b)). Finally, the results reveal that a more suitable testing approach should be used in the future for ductile adhesive instead of ENF tests.
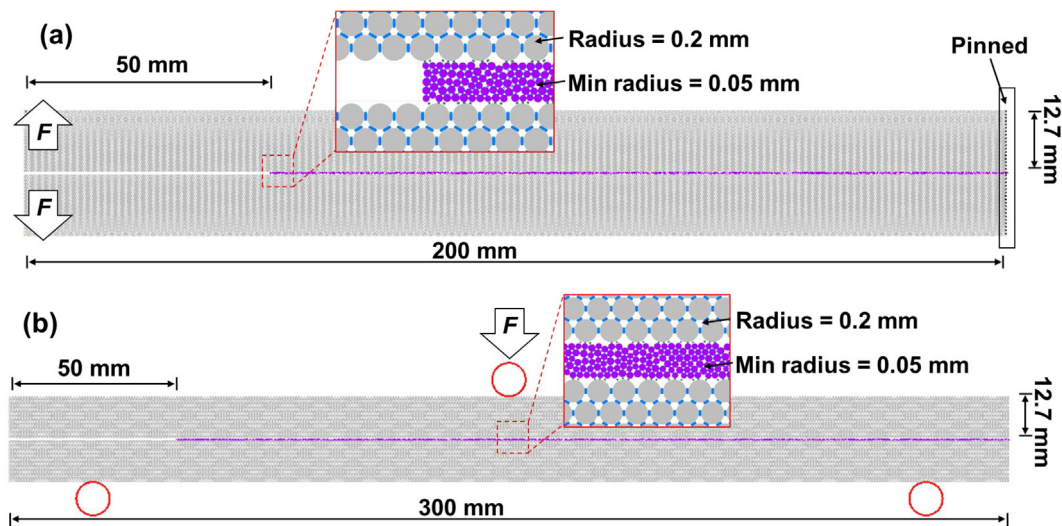
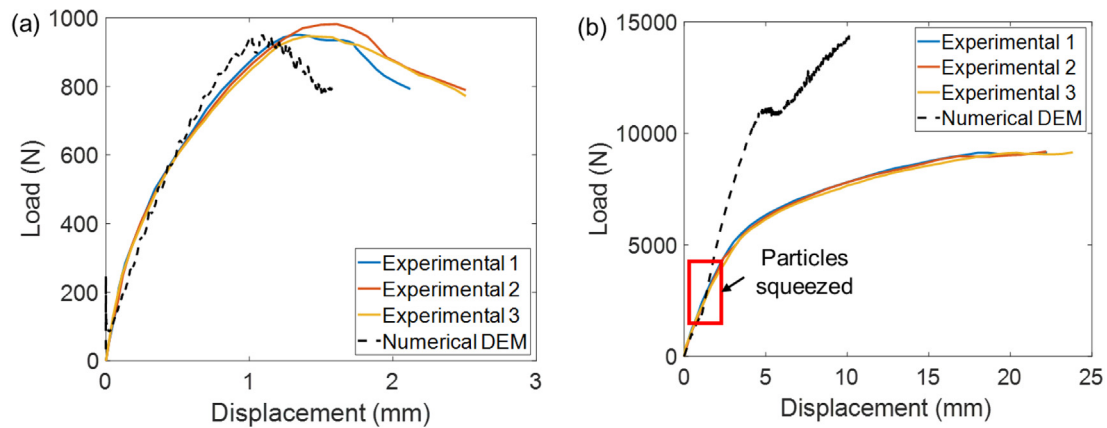**Fig. 13.** DE models of DCB and ENF tests: (a) DCB test, (b) ENF test.

Fig. 14. Comparison of experimental and numerical results: (a) DCB test, (b) ENF test. The red square box shows the initiation of particle squeezing under compression at the right end of bond line.

(2) SLJ tests with cohesive failure

However, the joints using a very soft and ductile adhesives are expected to sustain limited compressive actions. The tensile and shear actions are commonly more concerned in the joint designs or loading cases. Therefore, Teroson MS 9399 adhesive was then adopted to perform single lap joint (SLJ) tests, which were further used to validate the applicability of the develop DE model in simulating ductile adhesive joints with less compression action. The Teroson MS 9399 adhesive in SLJ is primarily subjected to combined shear and tensile action.

The model set up is given in Fig. 15(a). The adherend is made of AL material and the adhesive has a thickness of 0.56 mm. The numerical results were compared with those from the experiment as shown in Fig. 15(b). It can be seen that the load–displacement curves from DE modelling are highly consistent with those from lab tests. The validation with SLJ tests shows that the developed DE model is able to accurately predict the cohesive failure process and failure strength of the ductile adhesive joints. It can also support the conclusion that the incorrect prediction of observed failure process and load–displacement relationship in ENF test of the PU adhesive is due to the limitation of the adopted soft bond model in simulating the compressive action of soft materials. In addition, the parallel bond model which is frequently used in modelling the brittle fracture of materials such as rocks can be assigned with incompressible ability. However, it is very likely not suitable for simulating very soft materials with high elongation ratio at failure, which demands the softening behaviour of bonds.

(3) SLJ tests with adhesive failure

In addition to the validation of SLJ tests with cohesive failure, the adhesive failure might be traced using the developed DE model if other adherend materials are introduced. Thus, AL and PPA materials were adopted to make the dissimilar adherends of joints. The elastic modulus of PPA material is 17.6 GPa and PPA has a density of 1650 kg/m^3 with a tensile strength of 241 MPa. Its adhesion properties with Teroson MS 9399 were given in Table 5. Two types of SLJs, AL–PPA SLJ and PPA–PPA SLJ, were experimentally tested. The configuration of specimens was same as that of AL–AL SLJs. The results of lab tests show that PPA interface has a consistent adhesive failure mode (Fig. 16). Therefore, a parallel bond model which was able to reproduce the tested mean interfacial properties of PPA-adhesive was assigned to the adhesion interface. Although the parallel bond model does not have softening stage, the ductile joint behaviour can still be well simulated by the coupling performance of soft adhesive and parallel bonds.

Fig. 17 shows the comparison of load–displacement curves between numerical and experimental results. It can be found that the DE model can accurately predict the joint strength and its post-peak softening behaviour of AL–PPA SLJs (Fig. 17(a)). The adhesive failure mode can be observed from the numerical results. However, from Fig. 17(b), it seems that the numerical results overestimate the ultimate displacement of joint. Additional elastic modelling of the SLJ tests shows that the growth path of load–displacement curves before decohesion occurring from the DE results of PPA–PPA SLJ is reliable. Thus, the
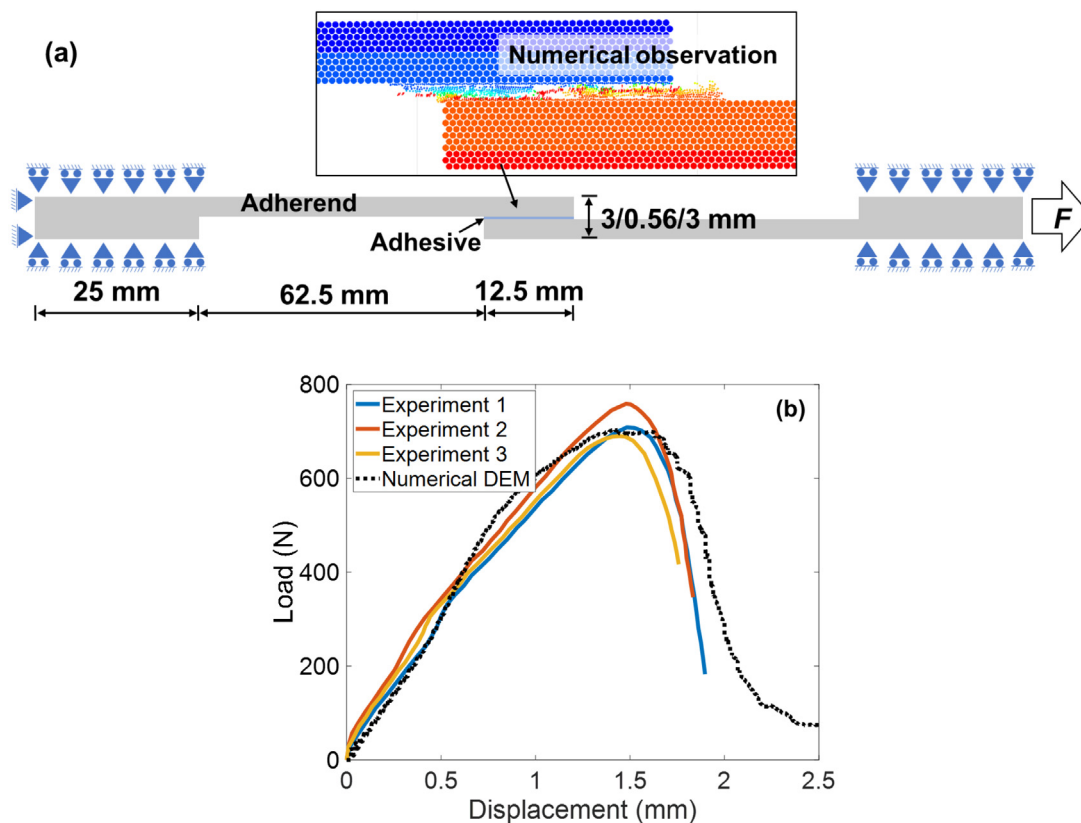
Fig. 15. SLJ model and the validation results: (a) the schematic of SLJ model and numerical observation, (b) load–displacement curves of numerical and experimental results.
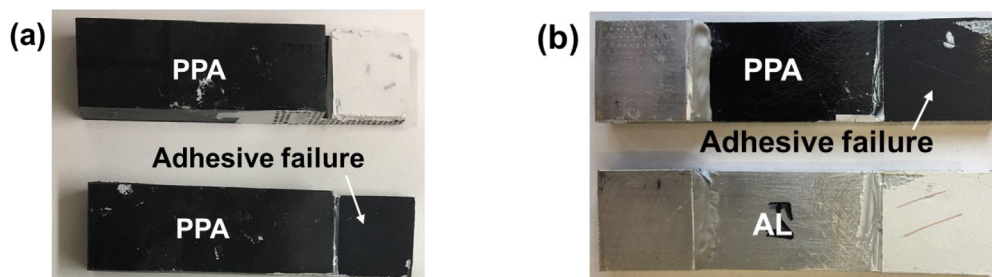

Fig. 16. Experimental observations of adhesive failure from PPA joints using Teroson MS 9399 adhesive: (a) PPA–PPA joining, (b) PPA–AL joining.

experimentally recorded displacement might have deviation as the peak displacement is relatively small and demands the testing procedure. Overall, the joint strength of PPA–PPA SLJs from DE simulation can still agree well with the testing data. The comparison results indicate that the developed DE model is able to describe both cohesive and adhesive failure of ductile adhesive joints.

4.4. Sensitivity study on adhesive thickness

In addition, the applicability of the proposed DE model in simulating the response variation of joints with different adhesive thicknesses is worthy investigated. Adhesive thickness has been reported to influence the fracture energies and further the joint performance, which cannot be adaptively captured using popular CZM models. CZM models require more lab tests to extract associated cohesive parameters for running the FE simulation. As the proposed model is expected to save these efforts with only validation once, the sensitivity of results on adhesive thickness was investigated. The variation of fracture energies and joint performance were examined in the following study.

(1) Fracture energies

The DE models for estimating the interlaminar-like properties in Fig. 10 were used to perform the sensitivity study of adhesive thickness on the fracture energies of Teroson MS 9399 joining. The tested adhesive thickness has a range of 0.1–1.0 mm. The extracted fracture energies in normal and tangential directions were given in Fig. 18. From Fig. 18(a), it is seen that the fracture energy in normal direction has a monotonous increase with greater adhesive thickness until the thickness reaches 1.0 mm. The lowest fracture energy corresponding to 0.1 mm thick adhesive is around 0.58 N/mm, whilst the fracture energy can see its peak (3.32 N/mm) with an adhesive thickness of 0.9 mm. Although the normal fracture energy declines at a thickness of 1.0 mm, additional sensitivity study on the particle randomness shows that this is very likely to be due to the limited deviation from random generation of adhesive particles. From Fig. 18(b), a similar trend of fracture energy growth can be found in the tangential direction. Differing from that in normal direction, the tangential fracture energy finds its peak at the adhesive thickness of 1.0 mm. The adhesive thicknesses of 0.4–0.5 mm and 0.6–0.7 mm are seen to present close results within each thickness interval. The numerical prediction of the
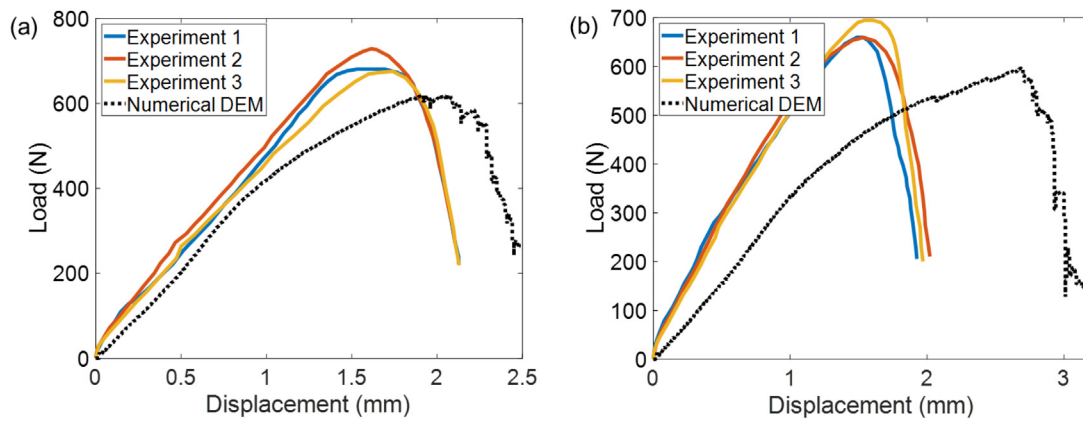
Fig. 17. Comparison of load–displacement results from DE simulation and lab tests: (a) AL–PPA SLJs, (b) PPA–PPA SLJs.
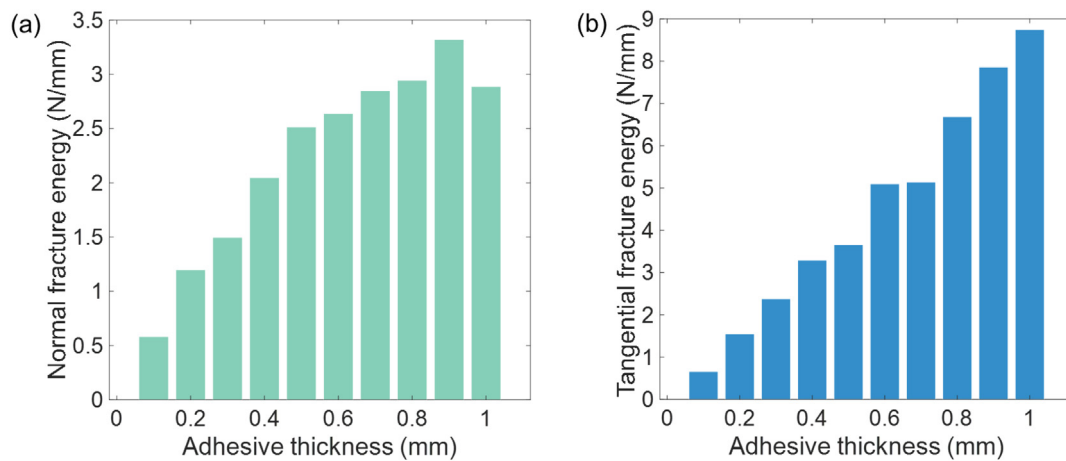

Fig. 18. The variation of fracture energies from different adhesive thicknesses: (a) Normal fracture energy, (b) Tangential fracture energy.

relationship between the adhesive thickness and fracture energy agrees well with those from current experimental reports. Taking the popular ductile adhesive Araldite®2015 as example, in Han's work [29], the experimental results show that the normal fracture energy can see a rise when adhesive thickness increases, whereas it has a drop at the thickness of 1.0 mm. As for the tangential direction, Figueiredo et al. [28] tested the fracture energy variation within the thickness range of 0.1–2.0 mm. The results indicate that the tangential fracture energy has a consistent rise from nearly 3 N/mm to over 10 N/mm within the thickness range of 0.1–1.0 mm, and that is likely to have a plateau within the range of 1.0–2.0 mm.

(2) Joints performance

The examined adhesive thickness ranges from 0.1 mm to 1.4 mm, at least five layers of particles were generated for the adhesive layer with very small thickness. AL–AL SLJs were selected to perform the sensitivity study of the adhesive thickness on the joint performance. In addition, the adherend stiffness was also treated as the investigated variable, which selected 10 GPa, 70 GPa and 200 GPa as the elastic modulus of adherend. The load displacement results associated with different adherend stiffness and adhesive thicknesses were shown in Fig. 19. It can be seen that in most occasions the joint strength does not see evident difference within the thickness range from 0.1 to 0.9 mm. The peak load ranges from nearly 680 N to 750 N, in which the highest joint strength is achieved by the smallest adhesive thickness. From above study, the smallest adhesive thickness has the lowest fracture energy, thus it can be found that the ductile joint strength is not controlled by the fracture energy. Instead, the cohesive fracture strength which does not see significant variation in above works is likely to contribute the most in determining the joint strength. The greater fracture energy

only affects the displacement at failure. From Fig. 19(a) and (c), it is seen that 1.4 mm thick adhesive results in different trends of joint strength with increasing the adherend stiffness. The joint strength from the adherend modulus of 10 GPa with a thickness of 1.4 mm is greater than that with 1.2 mm thick adhesive, whereas that from the adherend modulus of 200 GPa has an opposite decline. This might be caused by the influence of the adherend stiffness on the rotation angle at the joining area. The failure modes of SLJs with adherend modulus of 10 GPa and 200 GPa were given in Fig. 20 to better explain this issue. It can be seen that with a 1.4 mm thick adhesive, the SLJ with 10 GPa adherend modulus presents a greater relative transverse separation and larger rotation angle (see the bottom adherend), which refer to greater tensile action on adhesive, than that with 200 GPa adherend modulus. Combined with the footprints of the cohesive fractures of adhesive, it can be inferred that in the former SLJ the tensile action on the adhesive contributes more in resisting the load and further the joint strength. The latter SLJ has mostly the shear action near the upper adhesion interface, which dominants the failure propagation. In the other SLJs with lower adhesive thickness (take 0.1 mm, 0.4 mm, 0.9 mm as example, see Fig. 20), from the adhesive fracturing path and the rotation angle, the above difference cannot be well observed.

Overall, through the above sensitivity study, the applicability of the developed model in estimating the response variation due to the adhesive thickness can be identified. The validation results show a reliable trend of both the fracture energies and structural joint performance with the adhesive thickness predicted by the proposed model after calibration.
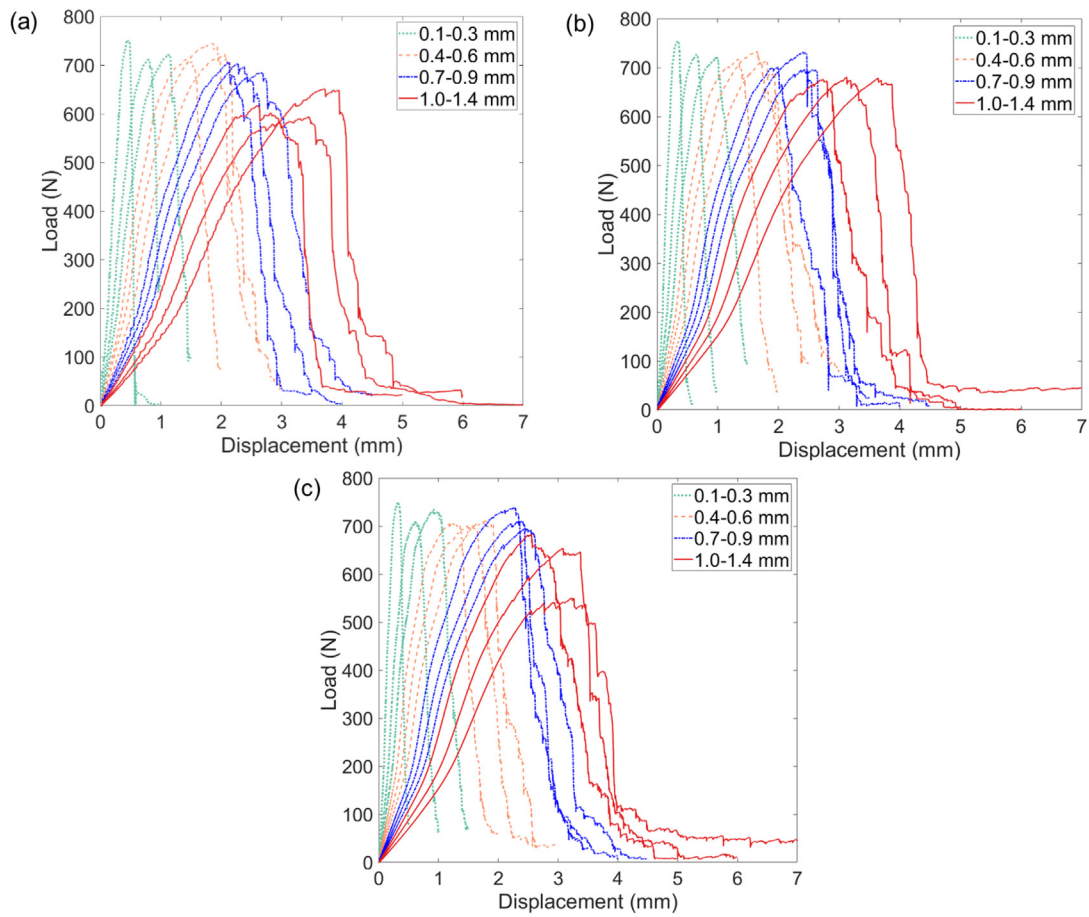
Fig. 19. Load displacement results from SLJs with different adherend stiffness and adhesive thicknesses: (a) Adherend material has an elastic modulus of 10 GPa, (b) 70 GPa, (c) 200 GPa.
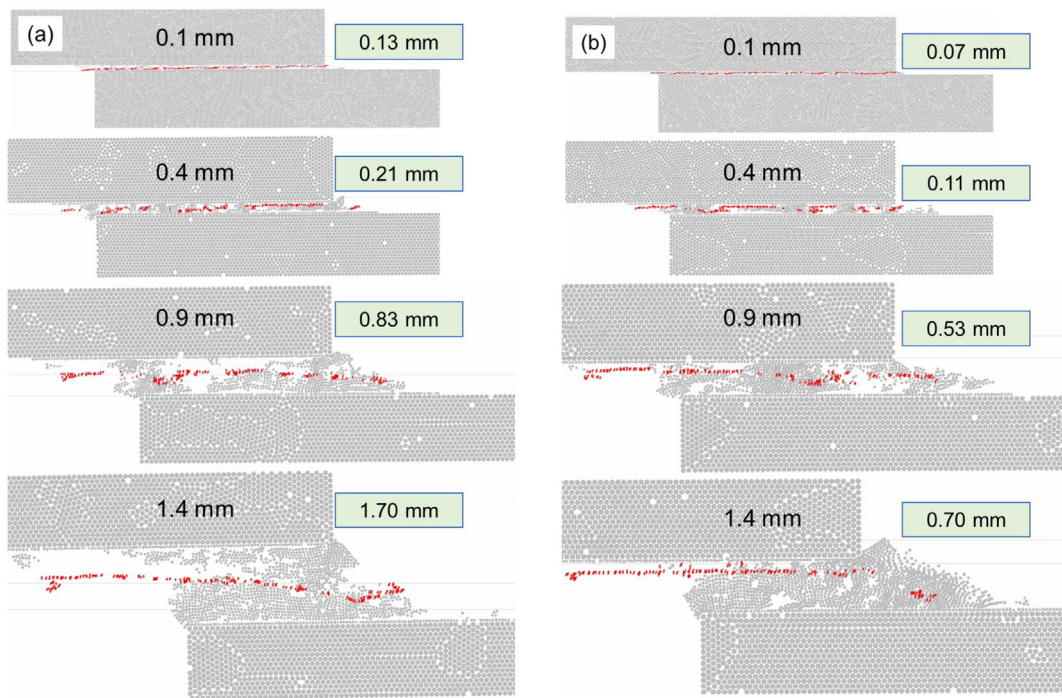

Fig. 20. Cohesive fractures of adhesives from SLJs with selected adhesive thicknesses, the transverse separation between the middle points of lap surfaces at the final step is given: (a) Adherend material has an elastic modulus of 10 GPa, (b) 200 GPa.

5. Conclusions

This work proposed a novel calibration strategy for developing a particle-based numerical model to simulate the ductile adhesive joints with robustness to suit various joint designs. It was based on a combined DE–GEP approach to promote the calibration of the microscale parameters of ductile adhesives. The symbolic regression models of bulk property and interlaminar-like property were developed. The calibration concept was also given to achieve the consistency of concerned properties.

The developed approach and symbolic regression models can be used to determine the complex parameter combinations to model the ductile adhesive joints in a more straightforward manner. This can save many efforts on determining appropriate microscale parameters to obtain consistent material and joint performance, as great difficulties would rise when many discrete element parameters were considered to simulate complex behaviours. The contribution of each parameters into the macroscopic properties was also given to improve the retuning works of calibration.

Taking the polyurethane adhesive (Teroson MS 9399) as example, several classic tests were conducted to validate the developed numerical model with the estimated parameters. Both strength and shortcomings of the calibrated model were shown. It is found that the limitation of soft bond model results in an incorrection prediction for the performance of joints using very soft adhesives under compressive actions. This is due to the particles cannot be assigned with separately high contact stiffness in a soft material using the soft bond model in the software. Despite of such limitation, the validation results from the single lap joints show that the developed DE model can well describe the large strain and nonlinearity of ductile adhesives as well as giving reliable prediction on the joint strength and different failure modes. Considering that the ductile adhesive joints are commonly designed to sustain tensile and shear loads, the modelling accuracy of the developed particle-based model in predicting the failure process and failure strength of adhesive joints can be guaranteed.

Furthermore, the developed DE model after the proposed calibration is able to adaptively model the variation of joint performance without performing more lab tests to extract the cohesive parameters, e.g., when the design variables such as adhesive thickness varies the proposed model can predict the realistic fracture energies and the corresponding joint performance. This eliminates the demand to experimentally determine the delamination properties from different adhesive thicknesses as first of this kind. The strength of DE model in simulating the microstructural response also provides a promising solution for digging the micromechanical behaviours of joints.

CRediT authorship contribution statement

Xing-er Wang: Writing – original draft, Investigation. **Armin Yousefi Kanani:** Validation, Investigation, Data curation. **Kai Pang:** Software, Formal analysis. **Jian Yang:** Writing – review & editing. **Jianqiao Ye:** Writing – review & editing, Supervision. **Xiaonan Hou:** Writing – review & editing, Supervision, Project administration, Investigation, Funding acquisition.

Declaration of competing interest

The authors declare that they have no known competing financial interests or personal relationships that could have appeared to influence the work reported in this paper.

Data availability

The data that has been used is confidential.

References

[1] A. Pascuzzo, A. Yudhanto, M. Alfano, G. Lubineau, On the effect of interfacial patterns on energy dissipation in plastically deforming adhesive bonded ductile sheets, Int. J. Solids Struct. 198 (2020) 31–40, http://dx.doi.org/10.1016/j.ijsolstr.2020.04.001.

[2] Y. Chen, M. Li, X. Yang, W. Luo, Damage and failure characteristics of CFRP/aluminum single lap joints designed for lightweight applications, Thin-Walled Struct. 153 (2020) 106802, http://dx.doi.org/10.1016/j.tws.2020.106802.

[3] J. Presse, B. Künkler, T. Michler, Stress-based approach for fatigue life calculation of multi-material connections hybrid joined by self-piercing rivets and adhesive, Thin-Walled Struct. 159 (2021) 107192, http://dx.doi.org/10.1016/j.tws.2020.107192.

[4] A. Wagih, R. Tao, G. Lubineau, Bio-inspired adhesive joint with improved interlaminar fracture toughness, Composites A 149 (2021) 106530, http://dx.doi.org/10.1016/j.compositesa.2021.106530.

[5] U.A. Khashaba, Dynamic analysis of scarf adhesive joints in CFRP composites modified with Al2O3-nanoparticles under fatigue loading at different temperatures, Composites A 143 (2021) 106277, http://dx.doi.org/10.1016/j.compositesa.2021.106277.

[6] A. Mohabeddine, G. Malik, J. Correia, N. Fantuzzi, A. De Jesus, J.M. Castro, et al., Comparison between brittle and ductile adhesives in CFRP/steel joints, Procedia Struct. Integr. 37 (2022) 1043–1048, http://dx.doi.org/10.1016/j.prostr.2022.02.043.

[7] Z. Jiang, Z. Fang, S. Wan, K. Xie, Mode-II fracture behavior evaluation for adhesively bonded pultruded GFRP/steel joint using four-point bending test, Thin-Walled Struct. 167 (2021) 108130, http://dx.doi.org/10.1016/j.tws.2021.108130.

[8] L. Liu, X. Wang, Z. Wu, T. Keller, Tension-tension fatigue behavior of ductile adhesively-bonded FRP joints, Compos. Struct. 268 (2021) 113925, http://dx.doi.org/10.1016/j.compstruct.2021.113925.

[9] G. Sun, X. Xia, X. Liu, Q. Luo, Q. Li, On quasi-static behaviors of different joint methods for connecting carbon fiber reinforce plastic (CFRP) laminate and aluminum alloy, Thin-Walled Struct. 164 (2021) 107657, http://dx.doi.org/10.1016/j.tws.2021.107657.

[10] J. Zhang, J. Wang, Z. Yuan, H. Jia, Effect of the cohesive law shape on the modelling of adhesive joints bonded with brittle and ductile adhesives, Int. J. Adhes. Adhes. 85 (2018) 37–43, http://dx.doi.org/10.1016/j.ijadhadh.2018.05.017.

[11] I.J. Sánchez-Arce, L.D.C. Ramalho, R.D.S.G. Campilho, J. Belinha, Material nonlinearity in the numerical analysis of SLJ bonded with ductile adhesives: A meshless approach, Int. J. Adhes. Adhes. 104 (2021) 102716, http://dx.doi.org/10.1016/j.ijadhadh.2020.102716.

[12] X. Liu, X. Shao, Q. Li, G. Sun, Experimental study on residual properties of carbon fibre reinforced plastic (CFRP) and aluminum single-lap adhesive joints at different strain rates after transverse pre-impact, Composites A 124 (2019) 105372, http://dx.doi.org/10.1016/j.compositesa.2019.03.018.

[13] I. Katsivalis, O.T. Thomsen, S. Feih, M. Achintha, Failure prediction and optimal selection of adhesives for glass/steel adhesive joints, Eng. Struct. 201 (2019) 109646, http://dx.doi.org/10.1016/j.engstruct.2019.109646.

[14] M.D. Banea, M. Rosioara, R.J.C. Carbas, L.F.M. da Silva, Multi-material adhesive joints for automotive industry, Composites B 151 (2018) 71–77, http://dx.doi.org/10.1016/j.compositesb.2018.06.009.

[15] F. Marchione, P. Munafò, Effect of thermal aging on the mechanical performance of timber-timber single-lap adhesive joints, Int. J. Adhes. Adhes. 108 (2021) 102883, http://dx.doi.org/10.1016/j.ijadhadh.2021.102883.

[16] P.F. Liu, X.Q. Peng, Z.Y. Guo, J.X. Leng, L. Jiao, Viscoelastic bilinear cohesive model and parameter identification for failure analysis of adhesive composite joints, Compos. Struct. 224 (2019) 111016, http://dx.doi.org/10.1016/j.compstruct.2019.111016.

[17] G. Zheng, Z. He, K. Wang, X. Liu, Q. Luo, Q. Li, et al., On failure mechanisms in CFRP/Al adhesive joints after hygrothermal aging degradation following by mechanical tests, Thin-Walled Struct. 158 (2021) 107184, http://dx.doi.org/10.1016/j.tws.2020.107184.

[18] J. Yang, Y. Wang, X-e. Wang, X. Hou, C. Zhao, J. Ye, Local bridging effect of fractured laminated glass with EVA based hybrid interlayers under weathering actions, Constr. Build. Mater. 314 (2022) 125595, http://dx.doi.org/10.1016/j.conbuildmat.2021.125595.

[19] F. Marchione, P. Munafò, Influence of high temperature exposure on the mechanical performance of double-lap adhesive joints between glass and aluminium adherends, Constr. Build. Mater. 299 (2021) 124268, http://dx.doi.org/10.1016/j.conbuildmat.2021.124268.

[20] A.W. Momber, L. Fröck, T. Marquardt, Effects of accelerated ageing on the mechanical properties of adhesive joints between stainless steel and polymeric top coat materials for marine applications, Int. J. Adhes. Adhes. 103 (2020) 102699, http://dx.doi.org/10.1016/j.ijadhadh.2020.102699.

[21] M. Lizner, E. Alabort, H. Cui, A. Pellegrino, N. Petrinic, On the rate dependent behaviour of epoxy adhesive joints: Experimental characterisation and modelling of mode I failure, Compos. Struct. 189 (2018) 286–303, http://dx.doi.org/10.1016/j.compstruct.2018.01.019.

[22] Wang. X-e, X.-H. Huang, J. Yang, X. Hou, Y. Zhu, D. Xie, Experimental and analytical study on the pre-crack impact response of thick multi-layered laminated glass under hard body impact, Int. J. Mech. Sci. 206 (2021) 106613, http://dx.doi.org/10.1016/j.ijmecsci.2021.106613.

[23] X.-H. Huang, X-e. Wang, J. Yang, Z. Pan, F. Wang, I. Azim, Nonlinear analytical study of structural laminated glass under hard body impact in the pre-crack stage, Thin-Walled Struct. 167 (2021) 108137, http://dx.doi.org/10.1016/j.tws.2021.108137.

[24] N.S. Hirulkar, P.R. Jaiswal, P. Alessandro, P. Reis, Influence of mechanical surface treatment on the strength of mixed adhesive joint, Mater. Today: Proc. 5 (9, Part 3) (2018) 18776–18788, http://dx.doi.org/10.1016/j.matpr.2018.06.224.

[25] R. Tao, M. Alfano, G. Lubineau, In situ analysis of interfacial damage in adhesively bonded composite joints subjected to various surface pretreatments, Composites A 116 (2019) 216–223, http://dx.doi.org/10.1016/j.compositesa.2018.10.033.

[26] M.N. Saleh, M.K. Budzik, M. Saeedifar, D. Zarouchas, S. Teixeira De Freitas, On the influence of the adhesive and the adherend ductility on mode I fracture characterization of thick adhesively-bonded joints, Int. J. Adhes. Adhes. 115 (2022) 103123, http://dx.doi.org/10.1016/j.ijadhadh.2022.103123.

[27] F. Sun, C.I. Pruncu, P. Penchev, J. Jiang, S. Dimov, B.R.K. Blackman, Influence of surface micropatterns on the mode I fracture toughness of adhesively bonded joints, Int. J. Adhes. Adhes. 103 (2020) 102718, http://dx.doi.org/10.1016/j.ijadhadh.2020.102718.

[28] J.C.P. Figueiredo, R.D.S.G. Campilho, E.A.S. Marques, J.J.M. Machado, L.F.M. da Silva, Adhesive thickness influence on the shear fracture toughness measurements of adhesive joints, Int. J. Adhes. Adhes. 83 (2018) 15–23, http://dx.doi.org/10.1016/j.ijadhadh.2018.02.015.

[29] X. Han, Y. Jin, L.F.M. da Silva, M. Costa, C. Wu, On the effect of adhesive thickness on mode I fracture energy - an experimental and modelling study using a trapezoidal cohesive zone model, J. Adhes. 96 (5) (2020) 490–514, http://dx.doi.org/10.1080/00218464.2019.1601087.

[30] P. Tsokanas, T. Loutas, G. Kotsinis, V. Kostopoulos, W.M. van den Brink, F. Martin de la Escalera, On the fracture toughness of metal-composite adhesive joints with bending-extension coupling and residual thermal stresses effect, Composites B 185 (2020) 107694, http://dx.doi.org/10.1016/j.compositesb.2019.107694.

[31] X. Huo, Q. Luo, Q. Li, G. Sun, Measurement of fracture parameters based upon digital image correlation and virtual crack closure techniques, Composites B 224 (2021) 109157, http://dx.doi.org/10.1016/j.compositesb.2021.109157.

[32] L. Sun, Y. Tie, Y. Hou, X. Lu, C. Li, Prediction of failure behavior of adhesively bonded CFRP scarf joints using a cohesive zone model, Eng. Fract. Mech. 228 (2020) 106897, http://dx.doi.org/10.1016/j.engfracmech.2020.106897.

[33] J. Ebadi-Rajoli, A. Akhavan-Safar, H. Hosseini-Toudeshky, L.F.M. da Silva, Progressive damage modeling of composite materials subjected to mixed mode cyclic loading using cohesive zone model, Mech. Mater. 143 (2020) 103322, http://dx.doi.org/10.1016/j.mechmat.2020.103322.

[34] G. Sun, Y. Wei, X. Huo, Q. Luo, Q. Li, On quasi-static large deflection of single lap joints under transverse loading, Thin-Walled Struct. 170 (2022) 108572, http://dx.doi.org/10.1016/j.tws.2021.108572.

[35] A. Ammar, W. Leclerc, M. Guessasma, N. Haddar, Discrete element approach to simulate debonding process in 3D short glass fibre composite materials: Application to PA6/GF30, Compos. Struct. 270 (2021) 114035, http://dx.doi.org/10.1016/j.compstruct.2021.114035.

[36] N. Abid, M. Mirkhalaf, F. Barthelat, Discrete-element modeling of nacre-like materials: Effects of random microstructures on strain localization and mechanical performance, J. Mech. Phys. Solids 112 (2018) 385–402, http://dx.doi.org/10.1016/j.jmps.2017.11.003.

[37] M. Marini, V. Fontanari, M. Benedetti, DEM/FEM simulation of the shot peening process on sharp notches, Int. J. Mech. Sci. 204 (2021) 106547, http://dx.doi.org/10.1016/j.ijmecsci.2021.106547.

[38] M. Dosta, K. Bistreck, V. Skorych, G.A. Schneider, Mesh-free micromechanical modeling of inverse opal structures, Int. J. Mech. Sci. 204 (2021) 106577, http://dx.doi.org/10.1016/j.ijmecsci.2021.106577.

[39] X-e. Wang, J. Yang, Q-f. Liu, Y-m. Zhang, C. Zhao, A comparative study of numerical modelling techniques for the fracture of brittle materials with specific reference to glass, Eng. Struct. 152 (2017) 493–505, http://dx.doi.org/10.1016/j.engstruct.2017.08.050.

[40] M. De Simone, L.M.S. Souza, D. Roehl, Estimating DEM microparameters for uniaxial compression simulation with genetic programming, Int. J. Rock Mech. Min. Sci. 118 (2019) 33–41, http://dx.doi.org/10.1016/j.ijrmms.2019.03.024.

[41] N.H.T. Nguyen, H.H. Bui, G.D. Nguyen, An approach to calculating large strain accumulation for discrete element simulations of granular media, Int. J. Numer. Anal. Methods Geomech. 44 (11) (2020) 1525–1547, http://dx.doi.org/10.1002/nag.3076.

[42] J. Rojek, A. Zubelewicz, N. Madan, S. Nosewicz, The discrete element method with deformable particles, Internat. J. Numer. Methods Engrg. 114 (8) (2018) 828–860, http://dx.doi.org/10.1002/nme.5767.

[43] R. Gibaud, É. Guesnet, P. Lhuissier, L. Salvo, Modeling large viscoplastic strain in multi-material with the discrete element method, Int. J. Mech. Sci. 136 (2018) 349–359, http://dx.doi.org/10.1016/j.ijmecsci.2017.12.044.

[44] P.A. Cundall, R.D. Hart, Numerical modelling of discontinua, Eng. Comput. 9 (2) (1992) 101–113, http://dx.doi.org/10.1108/eb023851.

[45] Itasca Consulting Group Inc., PFC — Particle Flow Code, Ver. 6.0, Itasca, Minneapolis, 2019.

[46] K. Tanaka, M. Nishida, T. Kunimochi, T. Takagi, Discrete element simulation and experiment for dynamic response of two-dimensional granular matter to the impact of a spherical projectile, Powder Technol. 124 (1) (2002) 160–173, http://dx.doi.org/10.1016/S0032-5910(01)00489-2.

[47] D.D. Shi, D. Cao, Y.B. Deng, J.F. Xue, DEM investigations of the effects of intermediate principal stress ratio and particle breakage on the critical state behaviors of granular soils, Powder Technol. 379 (2021) 547–559, http://dx.doi.org/10.1016/j.powtec.2020.10.094.

[48] H. Zhao, L. Han, Y. Liu, X. Liu, Quality prediction and rivet/die selection for SPR joints with artificial neural network and genetic algorithm, J. Manuf. Process. 66 (2021) 574–594, http://dx.doi.org/10.1016/j.jmapro.2021.04.033.

[49] K. Wu, H. Hu, L. Wang, Y. Gao, Parametric optimization of an aperiodic metastructure based on genetic algorithm, Int. J. Mech. Sci. 214 (2022) 106878, http://dx.doi.org/10.1016/j.ijmecsci.2021.106878.

[50] X-e. Wang, Y. Meng, J. Yang, X. Huang, F. Wang, H. Xu, Optimal kernel extreme learning machine model for predicting the fracture state and impact response of laminated glass panels, Thin-Walled Struct. 162 (2021) 107541, http://dx.doi.org/10.1016/j.tws.2021.107541.

[51] C. Mani, R. Karthikeyan, S. Kannan, C. Periasamy, Optimization of tensile properties of 316L stainless steel and Monel 400 weld joints using genetic algorithm, Mater. Today: Proc. 27 (2020) 2846–2851, http://dx.doi.org/10.1016/j.matpr.2020.01.250.

[52] Z. Gu, Y. Liu, D.J. Hughes, J. Ye, X. Hou, A parametric study of adhesive bonded joints with composite material using black-box and grey-box machine learning methods: Deep neuron networks and genetic programming, Composites B (2021) 108894, http://dx.doi.org/10.1016/j.compositesb.2021.108894.

[53] Y. Liu, Z. Gu, D.J. Hughes, J. Ye, X. Hou, Understanding mixed mode ratio of adhesively bonded joints using genetic programming (GP), Compos. Struct. 258 (2021) 113389, http://dx.doi.org/10.1016/j.compstruct.2020.113389.

[54] C. Ferreira, in: J. Kacprzyk (Ed.), Gene Expression Programming: Mathematical Modeling by an Artificial Intelligence, Springer, Netherlands, 2006.

[55] Q. Lu, S. Zhou, F. Tao, J. Luo, Z. Wang, Enhancing gene expression programming based on space partition and jump for symbolic regression, Inform. Sci. 547 (2021) 553–567, http://dx.doi.org/10.1016/j.ins.2020.08.061.

[56] X.-E. Wang, J. Yang, X. Huang, F. Wang, Y. Zhu, Voronoi-FDEM concept for modelling post-fracture response of progressively damaged structural glass, Eng. Comput. (2021) http://dx.doi.org/10.1007/s00366-021-01318-6.

[57] International Organization for Standardization, ISO 37: Rubber, Vulcanized or Thermoplastic - Determination of Tensile Stress–Strain Properties, Switzerland, 2017.

[58] Itasca Consulting Group Inc., Soft-Bond Model 2021, Available from: http://docs.itascacg.com/pfc700/common/contactmodel/softbond/doc/manual/cmsoftbond.html?node2576.

[59] International Organization for Standardization, ISO 37 Rubber, Vulcanized or Thermoplastic — Determination of Tensile Stress–Strain Properties, Genevo, 2017.

[60] M.-H. Kim, U.-I. Ri, H.-S. Hong, Y.-C. Kim, Comparative study of failure models for prediction of mixed-mode failure characteristics in composite adhesively bonded joint with brittle/Quai-brittle adhesive using finite element analysis, Int. J. Adhes. Adhes. 109 (2021) 102911, http://dx.doi.org/10.1016/j.ijadhadh.2021.102911.

[61] A.Y. Kanani, Y. Liu, D.J. Hughes, J. Ye, X. Hou, Fracture mechanisms of hybrid adhesive bonded joints: Effects of the stiffness of constituents, Int. J. Adhes. Adhes. 102 (2020) 102649, http://dx.doi.org/10.1016/j.ijadhadh.2020.102649.

[62] Y. Ismail, Y. Sheng, D. Yang, J. Ye, Discrete element modelling of unidirectional fibre-reinforced polymers under transverse tension, Composites B 73 (2015) 118–125, http://dx.doi.org/10.1016/j.compositesb.2014.12.024.